Effects of oxygen addition to argon glow discharges: A hybrid Monte Carlo-fluid modeling investigation

Annemie Bogaerts

University of Antwerp, Department of Chemistry, Research group PLASMANT, Universiteitsplein 1, B-2610 Wilrijk-Antwerp, Belgium

ABSTRACT

A hybrid model is developed for describing the effects of oxygen addition to argon glow discharges. The species taken into account in the model include Ar atoms in the ground state and the metastable level, O_2 gas molecules in the ground state and two metastable levels, O atoms in the ground state and one metastable level, O_3 molecules, Ar^+, O^+, O_2^+ and O^- ions, as well as the electrons. The hybrid model consists of a Monte Carlo model for electrons and fluid models for the other plasma species. In total, 87 different reactions between the various plasma species are taken into account. Calculation results include the species densities and the importance of their production and loss processes, as well as the dissociation degree of oxygen. The effect of different O_2 additions on these calculation results, as well as on the sputtering rates, is discussed.

© 2009 Published by Elsevier B.V.

1. Introduction

It is well known that glow discharges (GDs) applied for analytical spectrometry often contain small impurities of molecular gases, such as O_2 but also H_2 and N_2, besides the operating gas Ar [1]. Indeed, these molecular impurities arise due to contamination of the source by residual moisture or atmospheric gases, or by vapors from the pump oils. Furthermore, organic impurities can be adsorbed on the surface of the sample, or the molecular gases can simply be present as constituents in the sample. Oxide-based materials, especially as compacted powders, contribute oxygen from their natural composition, and they also add air and water to the discharge, trapped in the samples during the compacting process [2]. Bengtson [3,4] has demonstrated that organic or organometallic coatings, which find interest in the automotive industry, give rise to molecular emission, originating from OH, CH, NH and CO. These molecular bands overlap several atomic emission lines, causing line interferences. For good analytical practice, it is therefore highly important to obtain a better understanding of the effect of O_2 (and other) impurities in Ar glow discharges. This can be done by experiments (e.g., [1,5–9]) or by modeling.

Fischer et al. [5] investigated the influence of controlled additions of O_2 (and N_2) (in the range of 0–3 mass%) on sputtering rates, analyte emission intensities and electrical characteristics in an Ar dc GD. They observed a decrease in the sputtering rate with increasing concentration of O_2, resulting also in a drop for the emission intensities, reflecting the reduced atomic population in the plasma. The electrical current first increases with O_2 addition (until about 1.5%), and then it decreases or stays constant (depending on the metal investigated).

Wagatsuma [6] presented a review paper on the effect of Ar–He, Ar–O_2 and Ar–N_2 gas mixtures on GD-OES. In [7] the effects of O_2 addition, in the range of 0–100%, to an Ar GD were investigated. A significant drop in the emission intensity, discharge current and sputtering rate was observed for O_2 additions of a few %, followed by a minor rise at higher O_2 additions and a maximum around 50–60% O_2 concentration.

Fernàndez et al. investigated the effects of adding either H_2, N_2 or O_2 (in the range of 0.5–10%) to an Ar rf glow discharge used for OES [8,9]. Changes in the sputtering rate [8] and in the dc-bas voltage, the crater shapes and the depth resolution of thin films [9] were reported. The addition of the three molecular gases resulted in a decrease of the sputtering rate, compared to pure Ar. Concerning the emission yields, selective enhancements were observed for H_2 or N_2, but for O_2 addition in the range of 0.5–2%, a systematic increase of emission yields was found [8]. In [9] it was suggested that these plasma gas mixtures could offer a great potential to improve depth resolution in rf GDs.

Finally, Steers et al. [1] have reviewed the effects of traces of H_2, N_2 and O_2 on the electrical characteristics, the sputtering rate and the emission spectra in Ar glow discharges. The main emphasis was on the effects of H_2, but brief comments were also made to other gas mixtures. With respect to oxygen, it was demonstrated that 0.25% of O_2 addition yielded a slight change in the current–voltage characteristics, suggesting a small increase in plasma conductivity. Furthermore, Steers et al. reported recently also that O_2 addition resulted in a drastic decrease in sputtering rates, and hence in optical emission intensities of analyte species [10].

As mentioned above, in addition to experiments, it is also of interest to describe the effects of O_2 addition to Ar GDs by computer modeling. In

E-mail address: Annemie.bogaerts@ua.ac.be.

the literature there exist already several models for Ar/O$_2$, or pure O$_2$, discharges used for technological applications. Indeed, O$_2$ or Ar/O$_2$ plasmas are frequently used, for instance in the microelectronics industry for applications of oxidation, etching, cleaning, surface modification and thin film deposition [11]. Moreover, in magnetron discharges, Ar/O$_2$ gas mixtures are applied for the sputter-deposition of metal oxide thin films (e.g., [12,13]).

Trennepohl et al. [14] developed a collisional-radiative model for an Ar–O$_2$ magnetron discharge operating around 1 mTorr and relative O$_2$ concentrations varying from 0 to 100%. Balance equations were solved for Ar and for the molecular and atomic oxygen states, as well as for the positive and negative ions. The equations were coupled to the Boltzmann equation for the electron transport. The calculation results were compared with optical emission spectrometry. In [15] this model was further extended with a model for the interaction of the plasma species with various surfaces and for the consumption of the reactive gas. The calculations were performed for a relative O$_2$ concentration of 57%.

Nanbu et al. [16] presented a particle-in-cell Monte Carlo (PIC-MC) model for an Ar/O$_2$ dc magnetron discharge, operating at 5 mTorr and with an O$_2$ partial pressure varying from 30% to 70%. The model takes into account electrons, Ar$^+$ ions, O$^+$, O$_2^+$ and O$^-$ ions. A similar PIC-MC model, but with extended chemistry, describing also the sputtering and deposition process and the behavior of sputtered atoms and corresponding ions, as well as the O$_2$ molecules and O atoms, was developed by our group [17], for 1 Pa Ar pressure and O$_2$ partial pressures ranging from 0.02 to 0.24 Pa.

In [18] a very simple spatially-averaged model was presented for an Ar/O$_2$ rf magnetron source, at low O$_2$ flows (~0.5–2 sccm, for an Ar flow of 80 sccm) to study the deposition process of SiO$_x$ films. Only Ar ground state atoms, Ar$^+$ ions, O$_2$ and O species in the ground state and electrons were considered. Simple collisional-radiative models were also presented in [19] for a plasma free jet in an Ar/O$_2$ mixture, and in [20] for a low pressure Ar/O$_2$ discharge. A two-temperature chemically non-equilibrium model was developed in [21,22] for Ar/O$_2$ induction thermal plasmas at atmospheric pressure.

In [23] a radio-frequency non-equilibrium atmospheric pressure plasma in an Ar/O$_2$ mixture, at 6% O$_2$ concentration, was studied by experiments as well as by rate equations for the heavy species. The electron density and temperature obtained from literature were used as input in the model.

Lee and Lieberman presented a global (volume averaged) model for high-density plasmas in Ar, O$_2$, Cl$_2$ and in Ar/O$_2$ gas mixtures [24]. The pressure was varied from 1 to 50 mTorr. The O$_2$ fraction in the Ar/O$_2$ gas mixture was varied from 0 to 100%. The species taken into account are the Ar atoms in the ground state and one excited level, O$_2$ molecules, O atoms in the ground state and one excited level, Ar$^+$ ions, O$_2^+$, O$^+$ and O$^-$ ions. Hsu et al. [25] presented a fluid model for an inductively coupled plasma in pure Ar and mixtures of Ar and O$_2$ (or Ar/O$_2$/Cl$_2$) for pressures in the range of 10–80 mTorr, and O$_2$ concentrations chosen as 0, 37, 75 and 100%. The calculations were found in reasonable agreement with experiments, suggesting that the chemical reaction database assumed in the model is quite realistic.

Sommerer and Kushner [26] presented a hybrid Monte Carlo-fluid model for rf GDs in a wide range of gases, including O$_2$ as an example of an electronegative gas. Rauf and Kushner studied the behavior of Ar metastable atoms in Ar/O$_2$ cc rf discharges, also by means of a hybrid model [27]. The gas pressure was typically 250 mTorr and the O$_2$ partial pressure was in the order of 1%. In our group we used the same hybrid model to study the etch process in Ar/O$_2$/Cl$_2$ inductively coupled plasmas (at typical flow rates of 100 sccm Cl$_2$, 12 sccm Ar, and 0–14 sccm O$_2$) [28], as well as to investigate a pure O$_2$ plasma used for atomic layer deposition [29].

For pure O$_2$ plasmas, Elliasson and Kogelschatz presented a very detailed overview of all possible reactions [30], and they published a model based on this reaction set, for the O$_3$ generation in dielectric

barrier discharges [31]. Another model to calculate O$_3$ generation in an O$_2$-fed wire-to-cylinder ozonizer at atmospheric pressure was presented in [32]. In [33] a zero-dimensional (i.e., spatially-averaged) model was used to simulate a pulsed high-density O$_2$ discharge at 5 mTorr. It was found necessary to include the chemistry involving the high energy O$_2$ metastable molecules, in order to capture the experimentally observed increase in the O$^-$ density in the afterglow.

Gousset et al. [34] presented a model for the positive column of a low pressure dc discharge in O$_2$, in which the electron kinetics was coupled to the rate balance equations of the dominant heavy species, i.e., O$_2$ molecules in ground state and one excited level, ground state O atoms, O$_2^+$ and O$^-$ ions. The vibrational kinetics of the O$_2$ molecules was also taken into account. A similar basic approach was applied by Pinheiro et al. for a low pressure (0.1–5 Torr) surface wave discharge in flowing O$_2$, [35], but one more excited O$_2$ and O species, as well as the O$_3$ molecules were taken into account. Furthermore, the effect of the microwave nature of the sustaining field and the axial transport of the neutral species due to the gas flow were also accounted for. The measured electron density was used as an input in the model.

Guerra and Loureiro [36–38] developed a similar approach to study low pressure stationary N$_2$–O$_2$ discharges and microwave discharges, with special emphasis on the vibrationally excited N$_2$ and O$_2$ molecules [36]. In [37] the model was extended with electrons and positive ions, and in [38] the O$^-$ ions were also included. In a recent paper [39] it was, however, suggested that this model was not yet complete, at least for a post-discharge, illustrating the complexity of mixed N$_2$/O$_2$ plasmas. Also in [40] a very extensive kinetic scheme for non-equilibrium discharges in N$_2$/O$_2$ mixtures was developed, but for a vibrationally unexcited gas.

In the present paper, we have developed a hybrid Monte Carlo-fluid model for an Ar/O$_2$ GD, with typical O$_2$ concentrations in the range of 0.05–5%. The model is in first instance developed for analytical spectrometry applications, but it is of course generally valid for other plasma applications as well, when operating under similar conditions.

2. Description of the model

2.1. Species included in the model and short description of the Monte Carlo (MC) model and fluid model

The different species included in the model are listed in Table 1. For Ar, the atoms in the metastable level (3p^5 4 s ^{3}P$_2$, at 11.55 eV above the ground state; denoted as Ar$_m^*$) and the Ar$^+$ ions are considered, beside the Ar ground state atoms. For oxygen, the O$_2$ molecules in the ground state and in two excited (metastable) levels (at 0.977 and 1.627 eV) are included, as well as the O atoms in the ground state and in the lowest metastable level (at 1.97 eV above the ground state), and the O$_3$ molecules. Besides the O$_2^+$ and O$^+$ ions, also the negative ions O$^-$ are considered. Finally, of course also the electrons are taken into account.

The model developed in this work is a hybrid model, similar to the hybrid models we developed earlier for Ar/H$_2$ [41–43] and Ar/N$_2$ [44] GDs. It is based on a Monte Carlo (MC) model for the fast electrons,

Table 1
Different plasma species considered in the model.

Ground state neutrals	Neutrals in excited state	Ions	Electrons
Ar^0	Ar$_m^*$ (in metastable level)	Ar$^+$	e$^-$
O$_2$ (X) (X$^3\Sigma^-$)	O$_2$ (a) (a$^1\Delta_g$)	O$_2^+$	
O (^{3}P), O$_3$	O$_2$ (b) (b$^1\Sigma_g^+$)	O$^+$, O$^-$	
	O (^{1}D)		

For the O$_2$ molecules in ground and excited levels, the full notation is given between brackets, but further in this paper, only the short notations are used, i.e., O$_2$(X) (for the ground state) and O$_2$(a) and O$_2$(b) for the excited (metastable) levels, lying at 0.977 eV and 1.627 eV above the ground state, respectively. For the O atoms, only the ground state and one excited (metastable) level, at 1.97 eV above the ground state, are included.

and a fluid model for all other plasma species, including the slow electrons. The distinction between fast and slow electrons is made based on their energy. Indeed, if the energy is higher than the threshold for inelastic collisions (i.e., for the Ar/O_2 gas mixture taken as 1 eV) the electrons are considered "fast", and their behavior (including the collisions) is described in detail with a MC model. On the other hand, the electrons with lower energy do not take part in inelastic collisions; their role in the plasma is mainly to carry the electric current and to provide negative space charge, and therefore, they can as well be treated with a fluid model.

The fast electron MC model is based on solving Newton's equations for a large number of individual electrons, during successive time-steps. The probability of collision during these time-steps is calculated as:

$$Prob_{coll} = 1 - \exp(-\Delta s \Sigma(n\sigma_{coll}(E)))$$

where Δs is the distance traveled during the time-step; n and $\sigma_{coll}(E)$ are the densities of the target particles and the cross sections of the different collision types of the electrons with energy E. This formula yields a value between 0 and 1, which is compared with a random number in the interval [0,1]. If the probability is lower than this random number, no collision occurs, and the procedure is repeated during the next time-step. If the probability is higher, a collision occurs and the kind of collision is determined based on the partial collision probabilities and another random number. The collisions included in this MC model are presented in the next section. Subsequently, the new energy and direction after collision are calculated, again based on random numbers and scattering theory. More details about this MC procedure can be found e.g. in [45]. By following a large number of electrons in this way, their behavior can be statistically simulated.

When the (sum of kinetic and potential) energy of the electrons drops below the threshold for inelastic collisions, they are transferred to the fluid model. This model does not only treat the slow electrons, but also all other plasma species, as listed in Table 1. It includes a continuity equation for each plasma species:

$$\frac{\partial n_i}{\partial t} + \nabla \cdot J_i = S_i.$$

In this equation, n_i and J_i stand for the densities and fluxes of species i, and S_i represents the net production rate, determined by different production and loss terms, as defined by the reactions in Tables 2–4 (see a more detailed explanation below).

The flux term is calculated by a transport equation, based on diffusion and migration in the electric field, for the charged species:

$$J_i = \pm \mu_i n_i E - D_i \nabla n_i.$$

D_i and μ_i are the species diffusion coefficients and mobilities, respectively, and E represents the electric field. The $(+)$-sign in the first term applies to the positive ions, whereas the $(-)$-sign corresponds to negative ions and electrons. The mobilities of the various ions are calculated using the low electric field Langevin mobility expression [46]. The diffusion coefficients of the ions and electrons are calculated from their mobilities, using the Einstein relation. For the neutral species, diffusion coefficients are calculated with the Chapman–Enskog equation for binary gas systems, using characteristic Lennard–Jones parameters, adopted from [47,48].

These equations for all plasma species are solved together with Poisson equation, in order to obtain a self-consistent electric field distribution:

$$\nabla^2 V = \frac{e}{\varepsilon_0}[n_+ - n_- - n_e]$$

where n_+ and n_- are the (sum of the) positive and negative ion densities, respectively, and n_e is the electron density. The equations

are solved on a computational grid consisting of 60 grid points in the axial direction and 25 grid points in the radial direction. More details about the principle of this fluid model can be found e.g., in [49].

2.2. Electron impact reactions included in the model

Table 2 gives an overview of the electron reactions taken into account. Most of these reactions are treated in the electron MC model, and described by energy-dependent cross sections (denoted as $\sigma(E)$ in column 4). The collisions with Ar atoms (in ground state or metastable level) (i.e., Nos. 1–6), as well as the electron–electron Coulomb collision (No. 24), are the same as in our previous work (see plot of cross sections in Fig. 2(a) of Ref. [44]). The cross sections with oxygen species (i.e., Nos. 7–20 and 22) are plotted as a function of electron energy in Fig. 1. The labels to the curves of this figure correspond to the numbers in column 1 of Table 2.

Fig. 1(a) includes all collisions with O_2 molecules, except the various excitation collisions, which are depicted in Fig. 1(b). Note that electron impact excitation is considered to several excited levels, including $O_2(a)$ and $O_2(b)$, as well as the higher energy levels. The latter are not included explicitly in the model, because they are assumed to decay to the lower levels, but the corresponding excitation collisions needed to be included, as they cause significant energy loss for the electrons. In Table 2, these processes are summarized as excitation to higher O_2^* levels (No. 16), but this includes five different excitation processes, with energy losses taken equal to 4.5 eV, 6 eV, 8.4 eV, 9.97 eV and 14.7 eV, respectively. The cross sections of these individual processes are represented with dashed lines in Fig. 2(b). Vibrational and rotational excitation of the O_2 molecules are not taken into account, as these processes affect mainly the low energy part of the electron energy distribution function, and the MC model is only applied to the high energy electrons (so-called "fast electrons", able to produce ionization of the gas; cf. above). Moreover, the vibrationally excited levels of the O_2 molecules are not included in the model, because vibrational kinetics is not so important for O_2.

In Fig. 1(c) the cross sections of electron impact collisions with O atoms and O_3 molecules are plotted. For an accurate calculation of the electron energy distribution, not only electron impact excitation from the $O(^3P)$ ground state to the $O(^1D)$ level (No. 18) is included in the MC model, but also to the $O(^1S)$ level (reaction No. 19), but the latter species is not explicitly included in the model. Following ref. [40] the dissociation cross section of O_3 is taken as ten times the dissociation cross section of O_2 (i.e., reactions No. 10 and 11).

Apart from the electron impact collisions with O_2 ground state molecules, listed in Table 2, the same processes are also included for collisions with the O_2 molecules in the excited levels ($O_2(a)$ and $O_2(b)$), but the threshold of the collisions is then reduced, according to the energy of these levels (i.e., 0.98 eV and 1.63 eV, respectively). Moreover, also electron impact deexcitation from these levels to the ground state (or from $O_2(b)$ to $O_2(a)$) is taken into account, and the corresponding cross sections were obtained by the principle of detailed balancing. The same applies to deexcitation from the $O(^1D)$ level to the ground state.

Some of the electron reactions listed in Table 2, such as the various electron-ion recombinations, as well as attachment of O, dissociative attachment of O_3 and neutralization of O^-, occur at thermal energy. Therefore, they are not included in the MC model, but treated in the fluid model, with an overall rate coefficient, of which the value is given in column 4 of Table 2. T_e is given in K in reactions (25, 27 and 28) and in eV in reaction (30). In our model we assume $T_e = 1$ eV. The exact value of T_e is however not known. In principle, this can influence the calculations, because reactions (25, 27, 28 and 30 are dependent on T_e). However, the dependence of reactions (27, 28) is only minor, and reactions (25, 30) are found to exert a negligible effect on our

Table 2
Overview of the electron reactions included in the model, as well as the corresponding rate coefficients or cross sections, and the references where these data are adopted from.

No.	Reaction	Name	Rate coefficient or cross section	Ref.
1	$e^- + Ar \rightarrow e^- + Ar$	Momentum transfer with Ar	$\sigma(E)$	[50]
2	$e^- + Ar \rightarrow 2\,e^- + Ar^+$	Ionization of Ar	$\sigma(E)$	[50]
3	$e^- + Ar \rightarrow e^- + Ar^*$ (total)	Total excitation of Ar	$\sigma(E)$	[50]
4	$e^- + Ar \rightarrow e^- + Ar_m^*$	Excitation to Ar_m^*	$\sigma(E)$	[51]
5	$e^- + Ar_m^* \rightarrow 2\,e^- + Ar^+$	Ionization of Ar_m^*	$\sigma(E)$	[52]
6	$e^- + Ar_m^* \rightarrow e^- + Ar^*$ (total)	Total excitation from Ar_m^*	$\sigma(E)$	[53]
7	$e^- + O_2 \rightarrow e^- + O_2$	Momentum transfer with O_2	$\sigma(E)$	[54]
8	$e^- + O_2 \rightarrow 2e^- + O_2^+$	Ionization of O_2	$\sigma(E)$	[54]
9	$e^- + O_2 \rightarrow 2e^- + O^+ + O$	Dissociative ionization of O_2	$\sigma(E)$	[30]
10	$e^- + O_2 \rightarrow e^- + O\,(^3P) + O\,(^3P)$	Dissociation of O_2	$\sigma(E)$	[30]
11	$e^- + O_2 \rightarrow e^- + O\,(^3P) + O\,(^1D)$	Dissociative excitation of O_2	$\sigma(E)$	[30]
12	$e^- + O_2 \rightarrow O^- + O$	Dissociative attachment of O_2	$\sigma(E)$	[54]
13	$e^- + O_2 \rightarrow e^- + O^+ + O^-$	Dissociation of O_2 (ion pair formation)	$\sigma(E)$	[16]
14	$e^- + O_2 \rightarrow e^- + O_2\,(a)$	Electronic excitation of O_2 to $O_2\,(a\ ^1\Delta_g)$	$\sigma(E)$	[54]
15	$e^- + O_2 \rightarrow e^- + O_2\,(b)$	Electronic excitation of O_2 to $O_2\,(b\ ^1\Sigma_g)$	$\sigma(E)$	[54]
16	$e^- + O_2 \rightarrow e^- + O_2^*$	Electronic excitation of O_2 to higher O_2^*	$\sigma(E)$	[54]
17	$e^- + O \rightarrow e^- + O$	Momentum transfer with O	$\sigma(E)$	[55]
18	$e^- + O \rightarrow e^- + O\,(^1D)$	Electron impact excitation of $O\,(^3P)$ to $O\,(^1D)$	$\sigma(E)$	[56]
19	$e^- + O \rightarrow e^- + O\,(^1S)$	Electron impact excitation of $O\,(^3P)$ to $O\,(^1S)$	$\sigma(E)$	[56]
20	$e^- + O \rightarrow 2\,e^- + O^+$	Electron impact ionization of O	$\sigma(E)$	[56]
21	$e^- + O + M \rightarrow O^- + M$	Electron attachment to O	$k = 10^{-31}\ \mathrm{cm^6\,s^{-1}}$	[30,40]
22	$e^- + O_3 \rightarrow e^- + O_2\,(X) + O\,(^3P)$	Dissociation of O_3	$\sigma(E)$	[30,40]
23	$e^- + O_3 \rightarrow O^- + O_2\,(X)$	Dissociative attachment of O_3	$k = 10^{-11}\ \mathrm{cm^3\,s^{-1}}$	[40]
24	$e^- + e^- \rightarrow e^- + e^-$	Electron–electron Coulomb collisions	$\sigma(E)$	[57]
25	$e^- + Ar^+ + e^- \rightarrow Ar + e^-$	Three-body recombination with Ar^+	$k = 10^{-19}\ (T_e(K)/300)^{-4.5}\ \mathrm{cm^6\,s^{-1}}$	[58]
26	$e^- + O^+ + M \rightarrow O + M$	Three-body recombination with O^+	$k = 10^{-26}\ \mathrm{cm^6\,s^{-1}}$	[30]
27	$e^- + O_2^+ \rightarrow O\,(^3P) + O\,(^3P)$	Dissociative recombination with O_2^+	$k = 2 \times 10^{-7}\ (300/T_e(K))^{0.7}\ \mathrm{cm^3\,s^{-s1}}$	[30]
28	$e^- + O_2^+ \rightarrow O\,(^3P) + O\,(^1D)$	Dissociative recombination with O_2^+	$k = 2 \times 10^{-7}\ (300/T_e(K))^{0.7}\ \mathrm{cm^3\,s^{-1}}$	[30]
29	$e^- + O_2^+ + M \rightarrow O_2 + M$	Three-body recombination with O_2^+	$k = 10^{-26}\ \mathrm{cm^6\,s^{-1}}$	[30]
30	$e^- + O^- \rightarrow 2e^- + O$	Neutralization	$k = 2 \times 10^{-7}\ \exp(-5.5/T_e)\ \mathrm{cm^3\,s^{-1}}$	[23,33]

Note that M stands for a third body (either Ar or O_2).

Table 3
Overview of the chemical reactions taken into account in the model for the various ions, as well as the corresponding rate coefficients, and the references where these data were adopted from.

No.	Reaction	Name	Rate coefficient	Ref
Ar^+ reactions				
31	$Ar^+ + O_2 \rightarrow Ar + O_2^+$	Charge transfer	$k = 5 \times 10^{-11}\ \mathrm{cm^3\,s^{-1}}$	[27,59–62]
32	$Ar^+ + O_2\,(a) \rightarrow Ar + O_2^+$	Charge transfer	$k = 5 \times 10^{-11}\ \mathrm{cm^3\,s^{-1}}$	(a)
33	$Ar^+ + O_2\,(b) \rightarrow Ar + O_2^+$	Charge transfer	$k = 5 \times 10^{-11}\ \mathrm{cm^3\,s^{-1}}$	(a)
34	$Ar^+ + O \rightarrow Ar + O^+$	Charge transfer	$k = 6.4 \times 10^{-12}\ \mathrm{cm^3\,s^{-1}}$	[27]
35	$Ar^+ + O^- \rightarrow Ar + O$	Neutralization	$k = 2.7 \times 10^{-7}\ (300/T_g)^{0.5}\ \mathrm{cm^3\,s^{-1}}$	[24]
O^+ reactions				
36	$O^+ + O_2 \rightarrow O + O_2^+$	Charge transfer	$k = 2.1 \times 10^{-11}\ \mathrm{cm^3\,s^{-1}}$	[25]
37	$O^+ + O_2\,(a) \rightarrow O + O_2^+$	Charge transfer	$k = 2.1 \times 10^{-11}\ \mathrm{cm^3\,s^{-1}}$	[25]
38	$O^+ + O_2\,(b) \rightarrow O + O_2^+$	Charge transfer	$k = 2.1 \times 10^{-11}\ \mathrm{cm^3\,s^{-1}}$	[25]
39	$O^+ + Ar \rightarrow O + Ar^+$	Charge transfer	$k = 2.1 \times 10^{-11}\ \mathrm{cm^3\,s^{-1}}$	(a)
40	$O^+ + O_3 \rightarrow O_2^+ + O_2$	Ion conversion	$k = 1 \times 10^{-10}\ \mathrm{cm^3\,s^{-1}}$	[40]
41	$O^+ + O + M \rightarrow O_2^+ + M$	Ion conversion	$k = 1 \times 10^{-29}\ \mathrm{cm^6\,s^{-1}}$	[40]
42	$O^+ + O^- \rightarrow O + O$	Neutralization	$k = 2.7 \times 10^{-7}\ (300/T_g)^{0.5}\ \mathrm{cm^3\,s^{-1}}$	[25]
O_2^+ reactions				
43	$O_2^+ + Ar \rightarrow O_2 + Ar^+$	Charge transfer	$k = 2.1 \times 10^{-11}\ \mathrm{cm^3\,s^{-1}}$	(a)
44	$O_2^+ + O^- \rightarrow O_2 + O$	Neutralization	$k = 1.5 \times 10^{-7}\ (300/T_g)^{0.5}\ \mathrm{cm^3\,s^{-1}}$	[25]
45	$O_2^+ + O^- \rightarrow O + O + O$	Neutralization	$k = 2 \times 10^{-7}\ (300/T_g)^{0.5}\ \mathrm{cm^3\,s^{-1}}$	[30,35]
46	$O_2^+ + O^- + M \rightarrow O_3 + M$	Neutralization/Ozone formation	$k = 2 \times 10^{-25}\ (300/T_g)^{2.5}\ \mathrm{cm^6\,s^{-1}}$	[23]
O^- reactions				
47	$O^- + O_2 \rightarrow e^- + O_3$	Electron detachment/Ozone formation	$k = 5 \times 10^{-15}\ \mathrm{cm^3\,s^{-1}}$	[40]
48	$O^- + O_2\,(a) \rightarrow e^- + O_3$	Electron detachment/Ozone formation	$k = 3 \times 10^{-10}\ \mathrm{cm^3\,s^{-1}}$	[30, 38,40]
49	$O^- + O_2\,(b) \rightarrow e^- + O + O_2$	Electron detachment	$k = 6.9 \times 10^{-10}\ \mathrm{cm^3\,s^{-1}}$	[30,38,40]
50	$O^- + O \rightarrow e^- + O_2$	Electron detachment	$k = 3 \times 10^{-10}\ (300/T_g)^{0.5}\ \mathrm{cm^3\,s^{-1}}$	[25]
35	$O^- + Ar^+ \rightarrow O + Ar$	Neutralization	$k = 2.7 \times 10^{-7}\ (300/T_g)^{0.5}\ \mathrm{cm^3\,s^{-1}}$	[24]
42	$O^- + O^+ \rightarrow O + O$	Neutralization	$k = 2.7 \times 10^{-7}\ (300/T_g)^{0.5}\ \mathrm{cm^3\,s^{-1}}$	[25]
44	$O^- + O_2^+ \rightarrow O_2 + O$	Neutralization	$k = 1.5 \times 10^{-7}\ (300/T_g)^{0.5}\ \mathrm{cm^3\,s^{-1}}$	[25]
45	$O^- + O_2^+ \rightarrow O + O + O$	Neutralization	$k = 2 \times 10^{-7}\ (300/T_g)^{0.5}\ \mathrm{cm^3\,s^{-1}}$	[30,35]
46	$O^- + O_2^+ + M \rightarrow O_3 + M$	Neutralization/Ozone formation	$k = 2 \times 10^{-25}\ (300/T_g)^{2.5}\ \mathrm{cm^6\,s^{-1}}$	[23]

Note that the recombination reactions with electrons were already tabulated in Table 2, and are therefore not repeated here. T_g is the gas temperature, in K.
(a) Assumed in this work (see text).

calculation results, as will be demonstrated below. Hence, in our case, the choice of T_e appears not so critical. The references to the papers where the cross sections and rate coefficients were adopted from, can be found in column 5.

2.3. Ion reactions included in the model

The chemical reactions taken into account for the various ions are listed in Table 3. These reactions include asymmetric charge transfer and ion conversion for the positive ions, as well as neutralization with O^- ions. For the latter species also electron detachment and ozone formation can take place.

The rate coefficient for asymmetric charge transfer between Ar^+ ions and O_2 molecules has been reported in the order of 4.4×10^{-11}–5.8×10^{-11} cm^3 s^{-1} [27,59–62]. In our study, we assume an intermediate value of 5×10^{-11} cm^3 s^{-1}, but we have also performed calculations varying the rate coefficient in this reported range, and the calculated results were found to be no different. The rate coefficient for

Table 4
Overview of the chemical reactions considered in the model for the various neutral species, as well as the corresponding rate coefficients (k) or Einstein transition probabilities (A), and the references where these data were adopted from.

No.	Reaction	Name	Rate coefficient	Ref.
O$_2$ (a) reactions				
51	O_2 (a) + O_2 (X) → 2 O_2 (X)	Collis.deexcitation	$k = 6 \times 10^{-16}$ cm^3 s^{-1}	[30,35]
52	O_2 (a) + Ar → O_2 (X) + Ar	Collis.deexcitation	$k = 6 \times 10^{-16}$ cm^3 s^{-1}	(a)
53	O_2 (a) + O (^{3}P) → O_2 (X) + O (^{3}P)	Collis.deexcitation	$k = 7 \times 10^{-16}$ cm^3 s^{-1}	[40]
54	O_2 (a) + O_3 → 2 O_2 (X) + O (^{3}P)	Ozone destruction	$k = 5.2 \times 10^{-11}$ exp($-2840/T_g$) cm^3 s^{-1}	[30,35,63]
55	O_2 (a) + O_3 → O_2 (X) + O_3	Collis.deexcitation	$k = 4.6 \times 10^{-11}$ exp($-2810/T_g$) cm^3 s^{-1}	[32]
56	2 O_2 (a) → O_2 (b) + O_2 (X)	Level conversion	$k = 1.8 \times 10^{-19}$ (T_g/300)$^{3.8}$ exp($700/T_g$) cm^3 s^{-1}	[63]
57	O_2 (a) → O_2 (X) + hν	Radiative decay	$A = 3.7 \times 10^{-4}$ s^{-1}	[63]
O$_2$ (b) reactions				
58	O_2 (b) + O_2 (X) → O_2 (a) + O_2 (X)	Collis.deexcitation	$k = 4.3 \times 10^{-22}$ exp($-241/T_g$) cm^3 s^{-1}	[40]
59	O_2 (b) + O_2 (X) → 2 O_2 (X)	Collis.deexcitation	$k = 1 \times 10^{-16}$ cm^3 s^{-1}	[63]
60	O_2 (b) + Ar → O_2 (X) + Ar	Collis.deexcitation	$k = 1 \times 10^{-16}$ cm^3 s^{-1}	(a)
61	O_2 (b) + O (^{3}P) → O_2 (X) + O (^{1}D)	Collis.deexcitation	$k = 3.39 \times 10^{-11}$ exp($-4201/T_g$) cm^3 s$^{=1}$	[40]
62	O_2 (b) + O (^{3}P) → O_2 (a) + O (^{3}P)	Collis.deexcitation	$k = 8 \times 10^{-14}$ cm^3 s^{-1}	[40,63]
63	O_2 (b) + O_3 → 2 O_2 (X) + O (^{3}P)	Ozone destruction	$k = 1.5 \times 10^{-11}$ cm^3 s^{-1}	[30,35,63]
64	O_2 (b) → O_2 (X) + hν	Radiative decay	$A = 0.14$ s^{-1}	[63]
O (^{3}P) reactions				
65	O (^{3}P) + 2 O_2 (X) → O_3 + O_2 (X)	Ozone formation	$k = 6.4 \times 10^{-35}$ exp($663/T_g$) cm^6 s^{-1}	[30,35]
66	O (^{3}P) + O_2 (X) + Ar → O_3 + Ar	Ozone formation	$k = 1.9 \times 10^{-35}$ exp($1057/T_g$) cm^6 s^{-1}	[23,63]
67	2 O (^{3}P) + O_2 (X) → O_3 + O (^{3}P)	Ozone formation	$k = 2.15 \times 10^{-34}$ exp($345/T_g$) cm^6 s^{-1}	[30,35]
68	2 O (^{3}P) + O_2 (X) → 2 O_2 (X)	Recombination	$k = 2.45 \times 10^{-31}$ $T_g^{-0.63}$ cm^6 s^{-1}	[40]
69	2 O (^{3}P) + Ar → O_2 (X) + Ar	Recombination	$k = 2.45 \times 10^{-31}$ $T_g^{-0.63}$ cm^6 s^{-1}	(a)
70	O (^{3}P) + O_3 → O_2 (a) + O_2 (X)	Ozone destruction	$k = 1 \times 10^{-11}$ exp($-2300/T_g$) cm^3 s^{-1}	[30, 35]
71	O (^{3}P) + O_3 → 2 O_2 (X)	Ozone destruction	$k = 1.8 \times 10^{-11}$ exp($-2300/T_g$) cm^3 s^{-1}	[30,35]
72	O (^{3}P) + O (^{1}D) → 2 O (^{3}P)	Level conversion	$k - 8 \times 10^{-12}$ cm^3 s^{-1}	[30,35]
O (^{1}D) reactions				
72	O (^{1}D) + O (^{3}P) → 2 O (^{3}P)	Collis.deexcitation	$k = 8 \times 10^{-12}$ cm^3 s^{-1}	[23,30,35]
73	O (^{1}D) + O_2 (X) → O (^{3}P) + O_2 (X)	Collis.deexcitation	$k = 7 \times 10^{-12}$ exp($67/T_g$) cm^3 s^{-1}	[23,30,35,40]
74	O (^{1}D) + O_2 (X) → O (^{3}P) + O_2 (a)	Collis.(de)excitation	$k = 1 \times 10^{-12}$ cm^3 s^{-1}	[23,30,35]
75	O (^{1}D) + O_2 (X) → O (^{3}P) + O_2 (b)	Collis.(de)excitation	$k = 2.56 \times 10^{-11}$ exp($67/T_g$) cm^3 s^{-1}	[30,35,40]
76	O (^{1}D) + Ar → O (^{3}P) + Ar	Collis.(de)excitation	$k = 5 \times 10^{-12}$ cm^3 s^{-1}	[64]
77	O (^{1}D) + O_3 → O (^{3}P) + O_3	Collis.deexcitation	$k = 2.4 \times 10^{-10}$ cm^3 s^{-1}	[30,35]
78	O (^{1}D) + O_3 → 2 O_2 (X)	Ozone destruction	$k = 2.4 \times 10^{-10}$ cm^3 s^{-1}	[30,35]
79	O (^{1}D) + O_3 → 2 O (^{3}P) + O_2 (X)	Ozone destruction	$k = 1.2 \times 10^{-10}$ cm^3 s^{-1}	[30,35]
80	O (^{1}D) + O_3 → O_2 (X) + O_2 (a)	Ozone destruction	$k = 1.2 \times 10^{-10}$ cm^3 s^{-1}	[30,35]
O$_3$ reactions				
81	O_3 + M → O (^{3}P) + O_2 (X) + M	Ozone destruction	$k = 7.3 \times 10^{-10}$ exp($-11400/T_g$) cm^3 s^{-1}	[23,63]
54	O_2 (a) + O_3 → 2 O_2 (X) + O (^{3}P)	Ozone destruction	$k = 5.2 \times 10^{-11}$ exp($-2840/T_g$) cm^3 s^{-1}	[30,35,63]
55	O_2 (a) + O_3 → O_2 (X) + O_3	Collis.deexcitation	$k = 4.6 \times 10^{-11}$ exp($-2810/T_g$) cm^3 s^{-1}	[32]
63	O_2 (b) + O_3 → 2 O_2 (X) + O (^{3}P)	Ozone destruction	$k = 1.5 \times 10^{-11}$ cm^3 s^{-1}	[30,35,63]
70	O (^{3}P) + O_3 → O_2 (a) + O_2 (X)	Ozone destruction	$k = 1 \times 10^{-11}$ exp($-2300/T_g$) cm^3 s^{-1}	[30,35]
71	O (^{3}P) + O_3 → 2 O_2 (X)	Ozone destruction	$k = 1.8 \times 10^{-11}$ exp($-2300/T_g$) cm^3 s^{-1}	[30,35]
78	O (^{1}D) + O_3 → 2 O_2 (X)	Ozone destruction	$k = 2.4 \times 10^{-10}$ cm^3 s^{-1}	[30,35]
79	O (^{1}D) + O_3 → 2 O (^{3}P) + O_2 (X)	Ozone destruction	$k = 1.2 \times 10^{-10}$ cm^3 s^{-1}	[30,35]
80	O (^{1}D) + O_3 → O_2 (X) + O_2 (a)	Ozone destruction	$k = 1.2 \times 10^{-10}$ cm^3 s^{-1}	[30,35]
Ar$_m^*$ reactions				
5	Ar$_m^*$ + e$^-$ → Ar$^+$ + 2 e$^-$	Electron impact ionization	$\sigma(E)$	[52]
6	Ar$_m^*$ + e$^-$ → Ar* + e$^-$	Electron impact excitation	$\sigma(E)$	[53]
81	Ar$_m^*$ + e$^-$ → Ar$_r^*$ + e$^-$	Quenching by electrons	$k = 2 \times 10^{-7}$ cm^3 s^{-1}	[65]
82	Ar$_m^*$ + Ar$_m^*$ → Ar^0 + Ar$^+$ + e$^-$	Metastable–metastable collisions	$k = 6.4 \times 10^{-10}$ cm^3 s^{-1}	[65,66]
83	Ar$_m^*$ + Cu^0 → Ar^0 + Cu$^+$ + e$^-$	Penning ionization of Cu	$k = 2.6 \times 10^{-10}$ cm^3 s^{-1}	[67,68]
84	Ar$_m^*$ + Ar^0 → Ar^0 + Ar^0	Two-body collisions	$k = 2.3 \times 10^{-15}$ cm^3 s^{-1}	[69]
85	Ar$_m^*$ + 2 Ar^0 → Ar$_2^*$ + Ar^0	Three-body collisions	$k = 1.4 \times 10^{-32}$ cm^6 s^{-1}	[69]
86	Ar$_m^*$ + O_2 → Ar^0 + O + O	Quenching by dissociation of O_2	$k = 2.1 \times 10^{-10}$ cm^3 s^{-1}	[70–72]
87	Ar$_m^*$ + O → Ar^0 + O	Quenching by collision with O	$k = 4.1 \times 10^{-11}$ cm^3 s^{-1}	[27]

T_g is the gas temperature, in K.
(a) Assumed in this work (see text).
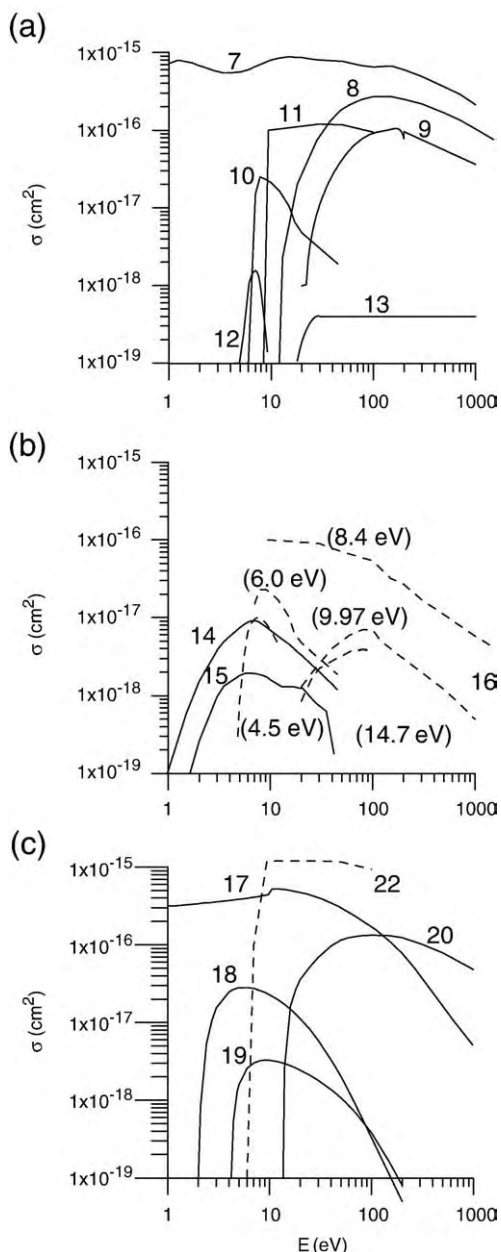
Fig. 1. Cross sections of the electron impact reactions with oxygen species, as a function of the electron energy. Part (a) shows all collisions with O_2 molecules, except for electron impact excitation, which is presented in part (b). Part (c) presents the collisions with O atoms (solid lines) and O_3 molecules (dashed lines). The labels of the curves correspond to the numbers of the reactions in the first column of Table 2.

asymmetric charge transfer between Ar^+ ions and O_2 molecules in the excited levels (a) and (b) is assumed to be the same as for the reaction with the ground state molecules, in accordance with [25].

Because no data could be found in literature for the rate coefficient of asymmetric charge transfer between O^+ ions and Ar atoms, the same value is assumed as for the reaction with O_2 molecules. The same applies for the charge transfer reaction between O_2^+ ions and Ar atoms. However, because both reactions can be important loss mechanisms for the O^+ and O_2^+ ions, the value of the rate coefficients was also varied in the range between 6×10^{-12} and 10^{-10} cm^3 s^{-1}, to check the effect of this assumption. It was found to affect only the O^+ and O_2^+ ion densities, respectively, but not the other calculated results (see Section 3 below).

Finally, reactions 35, 42 and 44–46 occur twice in the table, as they take place between two different ions (i.e., a positive ion and the O^-

ions). They are repeated explicitly for the O^- ions, for the sake of clarity and completeness.

2.4. Neutral reactions included in the model

Table 4 gives an overview of the chemical reactions included in the model for the various neutral species, i.e., the O_2 molecules in the metastable levels ($O_2(a)$ and $O_2(b)$), as well as the O atoms in the ground state and the metastable level ($O(^3P)$ and $O(^1D)$), the O_3 molecules and the Ar_m^* metastable atoms. The reactions of ground state O_2 molecules (i.e., $O_2(X)$) are not separately listed in the table, as they occur with all other reactive species, and are therefore listed already in this table and in previous Tables 2 and 3.

The reactions for the oxygen species include collisional excitation and deexcitation, level conversion, recombination, radiative decay, as well as ozone formation and destruction. Most rate coefficients could be found in literature, but for a few reactions, some assumptions had to be made (indicated with (a) in the table). For instance, the rate coefficients for deexcitation of the $O_2(a)$ and $O_2(b)$ levels upon collision with Ar atoms (i.e., reactions 52 and 60, respectively) are assumed the same as for the collisions with O_2 molecules (reactions 51 and 59, respectively). The same applies for the three-body reactions of $O(^3P)$ levels (reaction 69). The rate coefficient for deexcitation of $O(^1D)$ upon collision with Ar atoms (i.e., reaction 76) was reported to be in the range of 1×10^{-12}–2×10^{-11} cm^3 s^{-1} [64]. We have taken an intermediate value of 5×10^{-12} cm^3 s^{-1}, which is close to the value found for deexcitation upon collision with $O_2(X)$ molecules (i.e., reaction 73).

Reactions 57 and 64 are radiative decay from the $O_2(a)$ and $O_2(b)$ levels, respectively. They are characterized by the Einstein transition probabilities (A). The latter are, however, very low; hence radiative decay is not really important; it is only included here for the sake of completeness.

Note that reaction 72 is presented twice in the table, as it occurs between $O(^3P)$ and $O(^1D)$ atoms. Also the reactions involving O_3 (except for reaction 81) occur twice, because they happen between two different kinds of reactive species.

For the Ar_m^* metastable atoms, a number of reactions are included, which also take place in pure Ar discharges. Reactions 5 and 6 were also listed in Table 2. Note that quenching by electrons means the transfer of the metastable level to a nearby radiative level, which will decay to the ground state. The new reactions, occurring with oxygen species, and hence typical for the Ar/O_2 GD, are reactions 86 and 87.

2.5. Boundary conditions of the models

When the fast electrons in the MC model collide at the walls of the cell, they can be absorbed, reflected, or cause secondary electron emission, as defined by the reflection and secondary electron emission coefficient (see details in [45]). For the ion induced secondary electron emission, an effective emission coefficient of 0.15 is used, which includes the contributions of all the different ions. Indeed, this value was adopted, because it resulted in a realistic electrical current, as calculated by the model (see below). Such a procedure has been applied in other papers as well, because the exact values of the secondary electron emission yields for the various ions are often unknown. In principle, it is possible that the secondary electron emission yields vary due to the formation of an oxide layer on the metal cathode (i.e., so-called "target poisoning"; see also below), which results from the addition of O_2 to the Ar discharge. Consequently, this can influence the discharge characteristics, such as current–voltage profiles. From the experiments it is, however, not clear how the O_2 addition affects the electrical current. Indeed, some experiments reveal an initial increase in the current (up to about 1.5% O_2 concentration), followed by a drop or a constant behavior depending on the metal [5], whereas other experiments show the opposite trend, i.e., a drop in current for O_2 additions up to a few %,
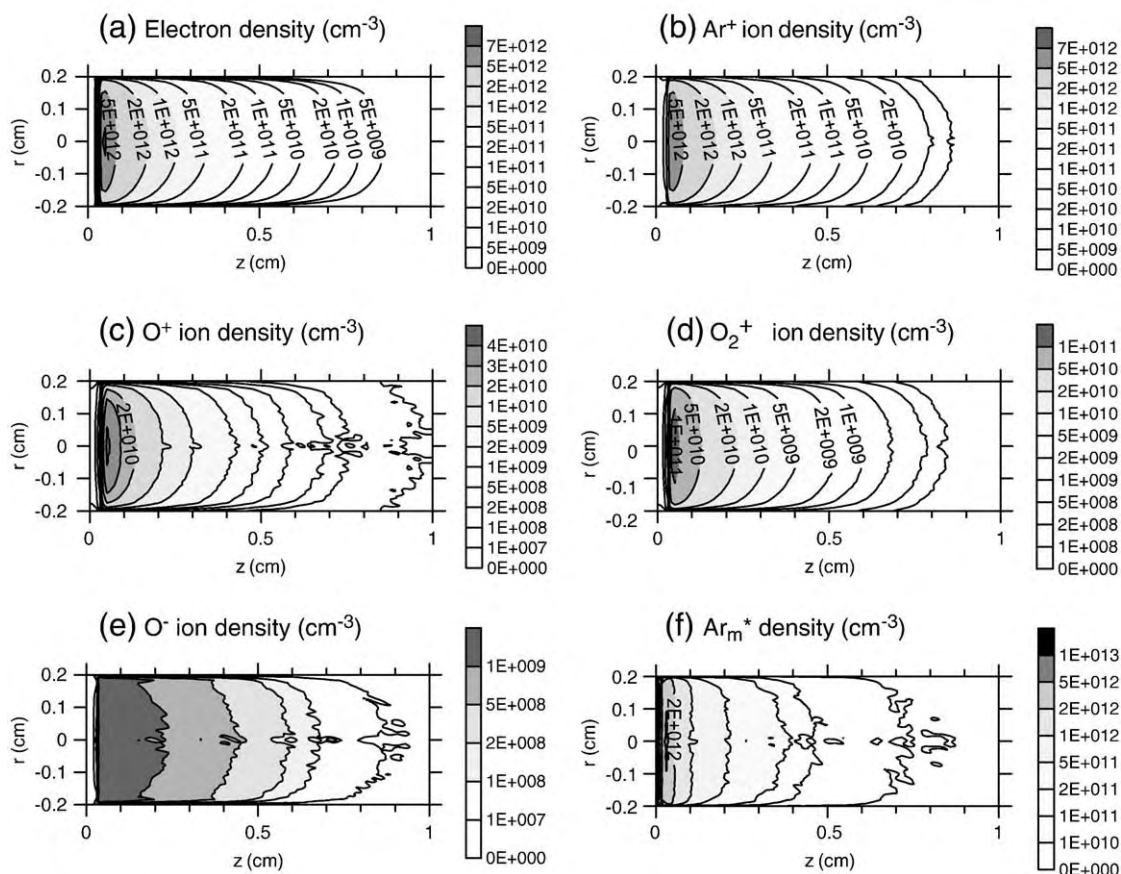
Fig. 2. Calculated 2D density profiles of the electrons (a), Ar$^+$ ions (b), O$^+$ ions (c), O$_2^+$ ions (d), O$^-$ ions (e) and Ar$_m^*$ metastable atoms (f), in a Grimm-type GD, at 850 Pa total gas pressure, 800 V dc discharge voltage, 13 mA electrical current, and 1% O$_2$ added to the discharge. The left axis represents the cathode, whereas the other figure borders are the cell walls, at anode potential. Only the first cm adjacent to the cathode is shown, as this is the most intense plasma region.

followed by a minor rise [7]. Finally, Steers et al. reported only a minor change in current–voltage characteristics [1]. Therefore, in the present study, we have treated the effective secondary electron emission yield as a constant value. This approach could be improved in future work, to investigate in more detail the effect of target poisoning on the discharge characteristics, if more experimental data become available.

In the fluid models, the electrons and negative ions are assumed to be lost at the walls (i.e., zero density at the walls). For the positive ions, the gradient of the density is taken as zero [49]. The excited species are assumed to be deexcited upon collision at the walls (i.e., zero density). Finally, the O atoms will undergo heterogeneous recombination at the walls, i.e., O + O + wall → O$_2$. The recombination coefficient was measured in [73] to be 0.07 for stainless steel and 0.27 for nickel. Guerra et al. [37] reported a value of 2×10^{-3} for a Pyrex surface. On the other hand, sticking coefficients of O atoms on pure metal surfaces in the order of 1 are also reported; however, this value typically drops when a metal oxide film is formed on the surface [17]. Kutasi and Loureiro [74] presented an extensive study about the effect of different N(^{4}S) and O(^{3}P) surface loss probabilities on the density distributions of various plasma species in an N$_2$–O$_2$ post-discharge, for three different wall materials, i.e., Pyrex, aluminium and stainless steel, based on data available in the literature. For O atoms, the values were varied in the range of 4×10^{-4}–2×10^{-3} for Pyrex; for aluminium the reported values were in the range of 2×10^{-3}–0.3, and for stainless steel, the values were in the range of 2×10^{-2}–0.17. The references where all these data were adopted from, are listed in Table 2 of [74]. In our model, we have assumed a recombination

coefficient of 0.07, but we have also performed simulations varying this parameter in the range between 0.002 and 1, to investigate the effect of this assumption (see below).

3. Results and discussion

The calculations are performed for a Grimm-type glow discharge source, operating at 800 V discharge voltage, 850 Pa total gas pressure, and about 13 mA electrical current. First, calculation results will be presented for an O$_2$ concentration of 1%. Both the 2D density profiles of the various plasma species, as well as the relative importance of their production and loss mechanisms, will be presented and discussed in the next section. In Section 3.2, the effect of different O$_2$ concentrations on the densities of the various plasma species, as well as on sputtering rates, will be investigated.

3.1. 1% O$_2$ concentration

3.1.1. Electrons

Fig. 2 presents the calculated 2D density profiles of the electrons, the various (positive and negative) ions, and the Ar$_m^*$ metastable atoms, at 1% O$_2$ addition in a Grimm-type source. Note that only the first cm adjacent to the cathode is represented in this figure, as this is the most intense plasma region [75].

The electron density (Fig. 2a) reaches a maximum of 7×10^{12} cm^{-3} at about 0.5 mm from the cathode (i.e., the beginning of the negative glow (NG) region), and decreases drastically further away from the

cathode, both in the axial and radial direction. This is due to the zero-density boundary conditions for the electrons at the cell walls, and also because the production mainly takes place in the beginning of the NG. Indeed, the production is mainly due to electron impact ionization of Ar (nearly 98%; see Table 5), which is most efficient in the beginning of the NG (e.g., [49]). Electron impact ionization of O_2 accounts for about 1% of the electron production, which is logical in case of 1% O_2 addition, because the cross sections of Ar and O_2 ionization are very similar. Electron impact dissociative ionization of O_2 contributes for about 0.3%, and the other process are even of lower importance.

With respect to the loss of electrons, on the other hand, Table 5 illustrates that the O_2 species play a predominant role. Indeed, recombination with Ar^+ ions is negligible (~0.008%) in spite of the higher Ar^+ ion density (see below), but instead, recombination with O^+ and O_2^+ ions, especially dissociative recombination, are very important. Indeed, dissociative recombination is generally characterized by higher rate coefficients (see e.g. also in [76]) and no third body is needed to satisfy both the energy and momentum conservation laws. In our case, dissociative recombination with O_2^+, leading either to two ground state (O ^{3}P) atoms (i.e., reaction 27 of Table 2) or to one ground state and one excited (O ^{1}D) atom (i.e., reaction 28 of Table 2), were found to be equally important (both ~19% contribution), which is logical because both processes are characterized by the same rate coefficients (see Table 2). Besides recombination with O_2^+ and O^+ ions, also electron impact dissociative attachment of O_2 (i.e., reaction 12 of Table 2) appears very important for the loss of electrons, with a contribution calculated to be 58%.

3.1.2. Ar^+ ions

The 2D Ar^+ ion density profile, presented in Fig. 2(b), looks very similar to the electron density profile of Fig. 2(a), except near the cathode, in the cathode dark space (CDS), where the electron density is virtually zero, and the Ar^+ ion density is non-zero, albeit small, leading to a strong positive space charge, and hence a large electric field in this region. Further, the Ar^+ ion density is a little bit lower than the electron density, because of the presence of O^+ and O_2^+ ions (see below) and the condition of quasi-neutrality in the NG region (i.e., total negative charge equals the total positive charge).

The Ar^+ ions are also mainly created by electron impact ionization, like in the case of the electrons, but charge transfer of O_2^+ or O^+ ions with Ar atoms also contribute for 1–2% (see Table 5). Vice versa, the Ar^+ ions are mainly lost by charge transfer with O_2 molecules (in ground state or in excited levels).

3.1.3. O^+ and O_2^+ ions

The O^+ and O_2^+ ions (Fig. 2(c, d)) exhibit a similar density profile as the Ar^+ ions, but they are about two orders of magnitude lower in density, which is logical because of the 1% O_2 concentration in the plasma, and the fact that the cross sections of (dissociative) ionization of Ar and O_2 are comparable. The calculated O_2^+ ion density is about twice the O^+ ion density, which corresponds to the ratio of the cross sections for ionization vs. dissociative ionization (cf. curves 8 and 9 of Fig. 1). Moreover, the O_2^+ ions are also created by other processes (see below).

The O^+ ions are mainly produced by electron impact dissociative ionization of O_2 (~90%). Electron impact ionization of O atoms contributes for about 6% and asymmetric charge transfer of Ar^+ ions with O atoms accounts for 3%. Electron impact dissociation of O_2, yielding the formation of O^+ and O^- ions, is found to be of minor importance. Concerning the loss of O^+ ions, asymmetric charge transfer with Ar atoms is found to be the most significant, with a contribution of almost 99%, whereas charge transfer with O_2 molecules contributes for 1%.

In contrast to the O^+ ions, the O_2^+ ions are mainly produced by asymmetric charge transfer of Ar^+ with O_2 (~nearly 73%) whereas electron impact ionization of O_2 accounts for 27%. This is of course due

to the higher O_2 density compared to the O density (see below), increasing the probability of Ar^+ charge transfer. Vice versa, charge transfer of O_2^+ ions with Ar constitutes the dominant loss mechanism for the O_2^+ ions, although recombination with electrons also contributes for a few %.

As mentioned in Section 2.3 above, the rate coefficients for asymmetric charge transfer of O^+ and O_2^+ ions with Ar atoms were assumed to be 2.1×10^{-11} cm^3 s^{-1}, i.e., the same as for the reaction of O^+ with O_2. However, to investigate the effect of this assumption, we have also varied these rate coefficients in the range between 6×10^{-12} and 5×10^{-11} cm^3 s^{-1}, which are reasonable limits for asymmetric charge transfer. The results indicated that this variation affects the O^+ and O_2^+ ion densities, respectively, because asymmetric charge transfer with Ar constitutes the major loss mechanisms for these ions (see Table 5). Therefore, an increase/decrease in the rate coefficients by a factor of 2 more or less resulted in a decrease/increase of the same order, for the ion densities. However, this effect turns out to be negligible for the other plasma species. Indeed, charge transfer was found to play only a minor role in the production of Ar^+ ions, as was illustrated in Table 5.

3.1.4. O^- ions

The calculated 2D density profile of the O^- ions is plotted in Fig. 2(e). It reaches a broad maximum in the NG, and drops also as a function of distance from the cathode, but not so drastically as for the other ions. The density is clearly lower than the positive ion and electron densities. This is in correlation with [14,16,17] where it was also reported for an Ar/O_2 magnetron discharge, in different Ar/O_2 gas ratios, that the O^- density was considerable lower than the electron and other ion densities, even for a pure O_2 discharge [14].

Production of the O^- ions is mainly due to electron impact dissociative attachment of O_2, and to a lesser extent by electron impact dissociation of O_2 (ion pair formation). The O^- ions are mostly lost by neutralization with Ar^+ ions (i.e., reaction 35 of Table 2).

3.1.5. Ar_m^* metastable atoms

Fig. 2(f) illustrates the 2D density profile of the Ar_m^* metastable atoms. It reaches a pronounced maximum adjacent to the cathode, due to fast Ar^+ ion and fast Ar atom impact excitation (i.e., $Ar^+_f/Ar^0_f + Ar \rightarrow Ar^+_s/Ar^0_s + Ar_m^*$; where the subscripts f and s denote fast and slow ions/neutrals, respectively). Indeed, these processes contribute together for almost 50%, and are hence almost equally important to electron impact excitation. This was also observed in our previous studies [76,77], and it was confirmed by experiments [78].

As far as the loss of Ar_m^* metastable atoms is concerned, several processes contribute, as is clear from Table 5. Quenching by O_2 molecules, resulting in dissociation of the latter, plays the most important role, with a contribution of almost 50%, followed by quenching due to collision with electrons, and by diffusion (and subsequent quenching at the walls). Compared with our previous modeling study on the Ar/N_2 GD [44] it appears that Ar_m^* quenching due to O_2 molecules is much more significant than quenching due to N_2 molecules. Indeed, at 1% N_2 added to the Ar GD, quenching due to the N_2 molecules contributed only for about 20% to the loss of the Ar_m^* atoms [44]. This can be explained by the rate coefficient, which is a factor of six larger for quenching by O_2 than for quenching by N_2 [70–72].

3.1.6. O_2 molecules and O atoms in the ground state

The 2D density profiles of the O_2 molecules and O atoms in the ground state are illustrated in Fig. 3(a, b). The O_2 molecules have a density in the order of 2×10^{15} cm^{-3}, which corresponds to 1% of the total gas density. They are characterized by a nearly uniform density profile, with a local minimum adjacent to the cathode. This is because of dissociation into O atoms. Indeed, the O atom density reaches a maximum at this position, as is clear from Fig. 3(b). The maximum O

Table 5
Calculated relative contributions of the most important production and loss processes for the various plasma species.

Production processes	%	Loss processes	%
Electrons			
Electron impact ionization of Ar (2)	97.6	Dissociative recombination with O_2^+ (27, 28)	38.5
Electron impact ionization of O_2 (8)	1.1	Dissociative attachment of O_2 (12)	58.1
Electron impact dissociative ionization of O_2 (9)	0.3	Three-body recombination with O_2^+ (29)	2.5
		Three-body recombination with O^+ (26)	0.9
Ar^+ ions			
Electron impact ionization (2)	97.2	Charge transfer with O_2 (31–33)	99.7
Charge transfer of O_2^+ with Ar (43)	0.9	Charge transfer with O (34)	0.3
Charge transfer of O^+ with Ar (39)	1.9		
O^+ ions			
Electron impact dissociative ionization of O_2 (9)	90.4	Charge transfer with Ar (39)	98.9
Electron impact ionization of O (20)	5.9	Charge transfer with O_2 (36–38)	1.0
Electron impact dissocation of O_2 (ion pair formation) (13)	0.7	Recombination with electrons (26)	0.1
Charge transfer of Ar^+ with O (34)	3.0		
O_2^+ ions			
Charge transfer of Ar^+ with O_2 (31–33)	72.6	Charge transfer with Ar (43)	97.5
Electron impact ionization of O_2 (8)	27.1	Recombination with electrons (27–29)	
Charge transfer of O^+ with O_2 (36–38)	0.2		2.5
O^- ions			
Electron impact dissociative attachment of O_2 (12)	95.1	Neutralization with Ar^+ (35)	95.3
Electron impact dissocation of O_2 (ion pair formation) (13)		Neutralization with O_2^+ (44, 45, 46)	1.6
	4.8	Neutralization with O^+ (42)	0.6
		Electron detachment of O (50)	2.1
Ar_m^* metastable atoms			
Electron impact excitation (4)	51.7	Quenching by O_2 (dissociation) (86)	46.6
Fast Ar^+ ion impact excitation	11.9	Quenching by electrons (81)	22.1
Fast Ar^0 atom impact excitation	36.4	Quenching by O (87)	0.5
		Diffusion	21.2
		Penning ionization of Cu (83)	5.3
		Metastable–metastable collisions (82)	1.1
		Electron impact excitation to higher levels (6)	3.0
O_2 (X) ground state molecules			
Charge transfer of O_2^+ with Ar	~100	Dissociation by quenching of Ar_m^* (86)	49.3
		Charge transfer of Ar^+ with O_2 (31)	17.8
		Electron impact dissociation (10)	5.7
		Electron impact dissociative excitation (11)	16.1
		Electron impact ionization (8)	6.3
		Electron impact dissociative ionization (9)	2.3
		Electron impact excitation (14, 15)	1.8
O (^{3}P) ground state atoms			
O_2(X) dissoc. by quenching of Ar_m^* (86)	65.9	Electron impact excitation (18, 19)	69.6
Collisional deexcitation of O(^{1}D) (72–77, 79)	10.7	Electron impact ionization (20)	29.9
Electron impact dissoc. excitation of O_2 (11)	10.5		
Electron impact dissoc. of O_2 (10)	7.3		
Electron impact dissoc. ionization of O_2 (9)	1.2		
Electron-O_2^+ dissoc. recombination (27, 28)	0.3		
Charge transfer of O^+ with Ar	3.6		
O_2(a) excited molecules			
Electron impact excitation from O_2(X) (14)	98.9	Electron impact excitation to O_2(b) (15)	~100
Excitation of O_2 by collision with O(^{1}D) (74)	1.1		
O_2(b) excited molecules			
Electron impact excitation from O_2(X) or O_2(a) (15)	58.7	Electron impact dissocative excitation (11)	46.2
Excitation of O_2 by collision with O(^{1}D) (75)	41.3	Electron impact dissociation (10)	13.3
		Electron impact ionization (8)	19.5
		Electron impact dissociative ionization (9)	5.2
		Electron impact deexcitation to O_2(a)	1.4
		Deexcitation upon collision with Ar (60)	9.7
		Deexcitation upon collision with O(^{3}P) (62)	3.9
O(^{1}D) excited atoms			
Electron impact dissociative excitation from O_2(X) (11)	96.9	Deexcitation upon collision with Ar (76)	86.8
Electron impact excitation from O(^{3}P) (18)	2.2	Deexcitation upon collision with O_2(X) (73–75)	12.8
Electron-O_2^+ dissociative recombination (28)	0.9		
O_3 molecules			
Three-body collision of O(^{3}P) with 2 O_2(X) (65)	48.7	Electron impact dissociation (22)	90.0
Three-body collision of O(^{3}P) with O_2(X) and Ar (66)	48.7	Electron impact dissociative attachment (23)	1.6
Three-body collision of 2 O(^{3}P) with O_2(X) (67)	2.2	Ozone destruction upon collision with O(^{1}D) (78–80)	8.0

The numbers between brackets after each production or loss process refer to the reactions listed in Tables 2–4.
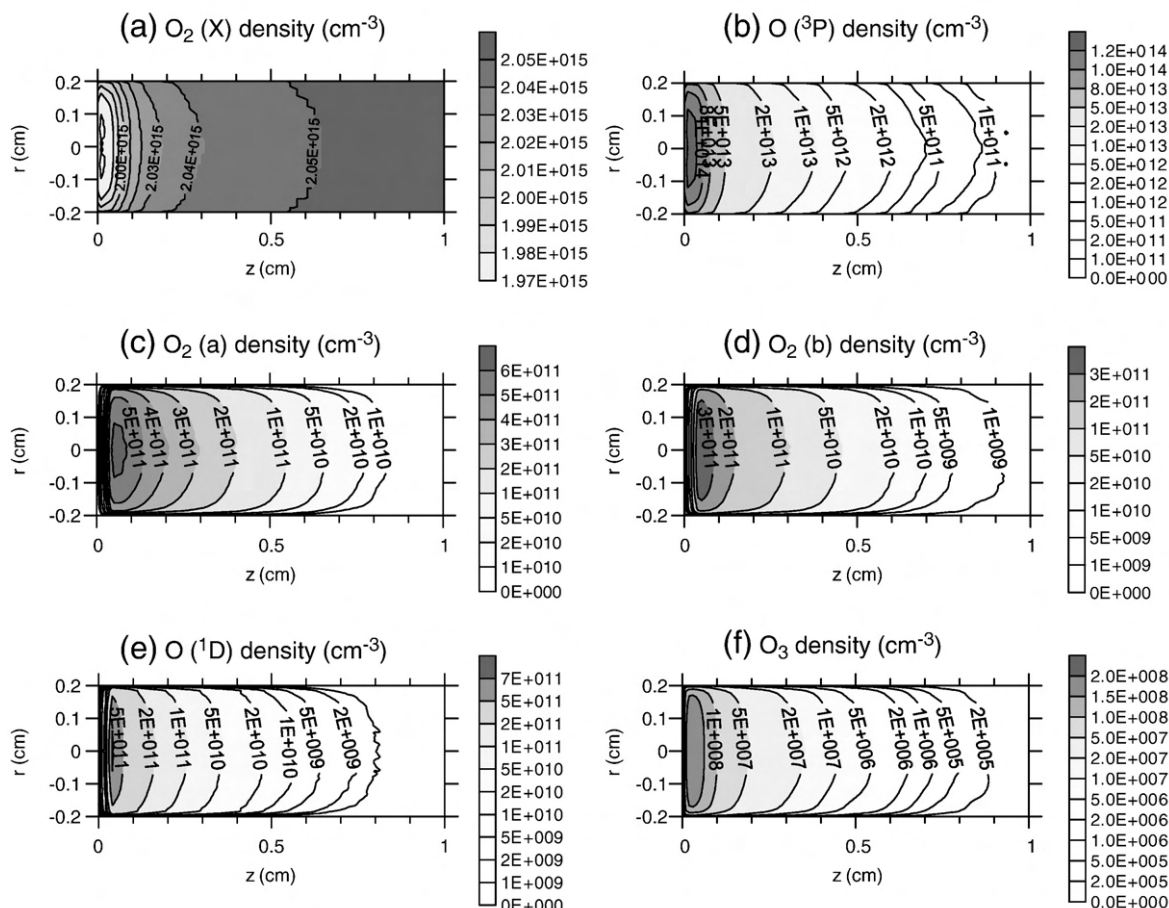
Fig. 3. Calculated 2D density profiles of the O$_2$(X) ground state molecules (a), O(^{3}P) ground state atoms (b), O$_2$(a) excited molecules (c), O$_2$(b) excited molecules (d), O(^{1}D) excited atoms (e), and O$_3$ molecules (f), in a Grimm-type GD, at the same conditions as in Fig. 2.

atom density is only about one order of magnitude lower than the O$_2$ density, but it drops quickly as a function of distance from the cathode.

Integrated over the entire discharge region, the dissociation degree was therefore calculated to be in the order of 1%. This is considerably lower than the dissociation degree of 10–30% reported by Kutasi et al. [79] for Ar/O$_2$ flowing microwave discharges and post-discharges. However, it is difficult to compare, because the plasma conditions are completely different. Other authors have reported dissociation degrees in the order of 10% for Ar/O$_2$ magnetron discharges [14], and even for pure O$_2$ surface wave discharges [35]. Compared with our previous studies on Ar/H$_2$ [41–43] and Ar/N$_2$ [44] GDs, the dissociation degree of O$_2$ is found to be comparable to the H$_2$ and N$_2$ dissociation degrees, for similar conditions.

Table 5 illustrates that the production of O$_2$ ground state molecules is almost exclusively due to asymmetric charge transfer of O$_2^+$ ions with the Ar gas. Nevertheless, this production process does not really affect the O$_2$ gas density, as it is negligible compared to the overall O$_2$ gas present in the discharge. The main loss mechanism appears to be dissociation by quenching of Ar$_m^*$ metastable atoms. This explains the dip in the O$_2$ gas density profile shown in Fig. 3(a), because it coincides with the pronounced maximum in the Ar$_m^*$ metastable atom density profile (Fig. 2(f)). Other processes, such as charge transfer of Ar$^+$ with O$_2$, electron impact dissociative excitation, dissociation, ionization, dissociative ionization and excitation, also contribute for several % to the loss of the O$_2$ gas molecules.

Most of the loss processes of the O$_2$ gas molecules result in the formation of the O(^{3}P) ground state atoms, such as dissociation of O$_2$ by Ar$_m^*$ quenching (which represents the dominant production process of the O(^{3}P) atoms), as well as electron impact dissociation,

dissociative excitation and ionization of O$_2$. Other important production processes for the O(^{3}P) atoms are collisional deexcitation of the O(^{1}D) excited atoms, as well as charge transfer of O$^+$ ions with Ar atoms. The loss of the O(^{3}P) atoms is almost entirely due to electron impact excitation and ionization.

As mentioned in Section 2.5 above, the O atoms will recombine at the walls, with the formation of O$_2$ molecules (i.e., O + O + wall → O$_2$), with a certain recombination probability. In our simulations, we have assumed a value of 0.07, which was reported in [73] for a stainless steel surface. However, because this value is subject to uncertainties and is moreover dependent on the material and the surface conditions, as discussed in Section 2.5 above, we have also performed calculations, varying this value from 0.002 to 1. The resulting 1D density profiles of the O(^{3}P) atoms are plotted in Fig. 4(a). The O$_2$(X) densities are not plotted, as they are virtually not affected by the assumed surface recombination probability. It is found that a higher recombination probability yields lower O densities, but the variation is less than a factor of two, for a variation in surface recombination probability of 500. Furthermore, from the O(^{3}P) and O$_2$(X) densities, integrated over the entire discharge, the dissociation degree can be calculated and this value is plotted in Fig. 4(b) against the value of the recombination probability. Changing the latter parameter between 0.002 and 1 results in a calculated dissociation degree varying between 0.9% and 0.6%, hence also a small variation.

3.1.7. O$_2$(a) and O$_2$(b) excited molecules
Fig. 3(c, d) depict the 2D density profiles of the O$_2$ molecules in the excited levels (O$_2$(a) and O$_2$(b)). They exhibit very similar density profiles, with a maximum in the beginning of the NG, due to electron
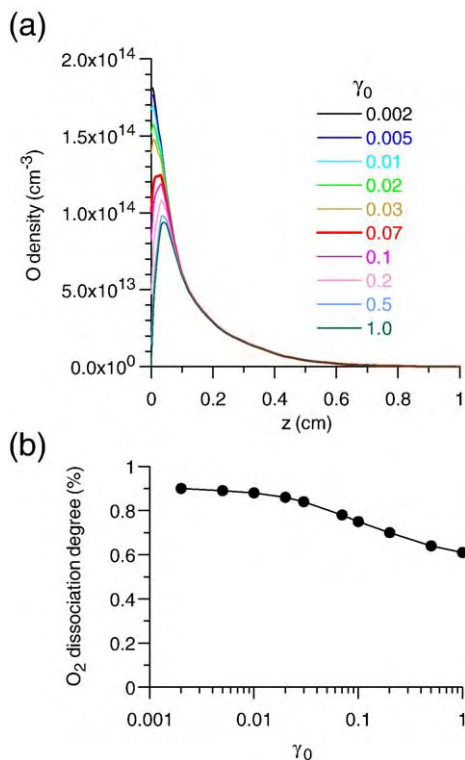
Fig. 4. Calculated 1D density profiles of the O(^{3}P) ground state atoms, at the same conditions as in Fig. 2, for different values of the surface recombination probability (O + O + wall → O$_2$) (a), and calculated O$_2$ dissociation degree as a function of the surface recombination probability (b).

impact excitation from the O$_2$(X) ground state molecules. Indeed, this process is a very important production mechanism for these levels. It is by far the dominant production mechanism for the O$_2$(a) levels, with a contribution of nearly 99%. Excitation of O$_2$(X) upon collision with O(^{1}D) atoms accounts for the remaining 1%. The situation is a bit different for the O$_2$(b) levels, where excitation of O$_2$ upon collision with O(^{1}D) atoms contributes for as much as 41%, whereas electron impact excitation, from both the O$_2$(X) ground state and the O$_2$(a) excited state, is responsible for about 59% of the O$_2$(b) production.

The latter process, i.e., electron impact excitation from the O$_2$(a) to the O$_2$(b) excited level appears by far the dominant loss mechanism for the O$_2$(a) level. This is because of the small energy difference between both energy levels, making this process already possible at relatively low energies. Other loss mechanisms, such as electron impact dissociation, (dissociative) ionization and dissociative excitation, as well as collisional deexcitation from the O$_2$(a) level, were found to be negligible compared to excitation to the O$_2$(b) level, because of much higher energies required.

On the other hand, these processes are found to be quite important for the loss of the O$_2$(b) level, as appears from Table 5, i.e., electron impact dissociative excitation, ionization, dissociation and dissociative ionization are found to contribute by 46%, ~20%, 13% and 5%, respectively. Indeed, there is no higher O$_2$ metastable level included in the model, and excitation to higher radiative levels is not considered as a loss process, because it is assumed that these levels can decay back to the lower level. Electron impact deexcitation from the O$_2$(b) level to the O$_2$(a) level accounts only for 1% to the loss of the O$_2$(b) levels. On the other hand, deexcitation of O$_2$(b) to the ground state, upon collision with either Ar or O(^{3}P) atoms, play a non-negligible role as loss mechanism for the O$_2$(b) level.

3.1.8. O(^{1}D) excited atoms

The O(^{1}D) atomic excited level exhibits a similar spatial profile as the O$_2$(a) and O$_2$(b) excited levels, with a pronounced maximum in the beginning of the NG. The O(^{1}D) maximum density is slightly higher than the O$_2$(a) and O$_2$(b) maximum densities, but it drops a bit more rapidly as a function of distance from the cathode. This similar profile is like expected, as the dominant production mechanism for the O(^{1}D) level is also given by electron impact excitation (more specifically: dissociative excitation) from the O$_2$(X) gas molecules. Also electron impact excitation from the O(^{3}P) ground state atoms and electron-O$_2^+$ dissociative recombination contribute for 1–2% to the production of the O(^{1}D) level. The most significant loss mechanism is deexcitation to the O(^{3}P) ground state, upon collision with Ar atoms, which accounts for 87%. Deexcitation upon collision with O$_2$(X) ground state molecules accounts for nearly 13%, mainly with the formation of O$_2$(b) excited levels (i.e., reaction 75 of Table 4); the latter process was indeed found to be quite important in the production of the O$_2$(b) levels (see above).

3.1.9. O$_3$ molecules

Finally, Fig. 3(f) presents the O$_3$ gas density profile. It is characterized by a similar profile as the O(^{3}P) ground state atoms (Fig. 3(b)). Indeed, it is mainly produced from the O(^{3}P) atoms, in a three-body collision with either two O$_2$(X) molecules, or one O$_2$(X) molecule and one Ar atom. Also a three-body collision with two O(^{3}P) atoms and one O$_2$(X) molecule has a minor contribution.

The density of the O$_3$ molecules is several orders of magnitude lower than for the other species, because three-body collisions are not so efficient at the rather low pressure under study (850 Pa). Moreover, O$_3$ molecules easily get lost by several mechanisms. The most important loss mechanism is electron impact dissociation (90%), followed by ozone destruction upon collision with O(^{1}D) molecules (reactions 78–80 each contribute for a few %).

3.2. Effect of O$_2$ concentration

We have investigated the effect of different O$_2$ additions on the calculation results, in the range of 0.05–5%. The densities of the various species are plotted against O$_2$ concentration in Fig. 5. Note that the density values are taken at the discharge axis, and averaged over the axial direction. Averaging over the radial direction is not done, as the radial variation is not so pronounced, except close to the cell walls, and moreover, the values near the cell axis are the most interesting ones. A logarithmic scale is applied for both the *x*-axis and the *y*-axis, to clearly visualize the effect of different O$_2$ concentrations, and to obtain an overall picture on the relative importance of the various species in the plasma.

It is clear that the Ar ground state gas atoms are characterized by the highest density in the plasma, followed by the O$_2$(X) gas molecules. Besides these two background gases, the O (^{3}P) ground state atoms are present at a large concentration, which is about two orders of magnitude lower than the O$_2$(X) ground state molecules. This gives rise to a dissociation degree in the order of a few %, decreasing upon higher O$_2$ concentrations, as is illustrated in Fig. 6. Note that the calculated dissociation degree is clearly higher when averaging the O and O$_2$ densities only over the axial direction, compared to averaging over the entire discharge. Indeed, in the first case, the density values are taken at the cell axis. As the O density drops in the radial direction to lower values at the cell walls, whereas the O$_2$ density is fairly uniform in the radial direction and is even slightly higher at the cell walls, it is logical that averaging over the entire discharge yields lower values for the dissociation degree.

The fact that the dissociation degree drops for higher O$_2$ concentrations is attributed to the decreasing role of Ar$_m^*$ quenching, which was found the dominant dissociation mechanism (see above and Table 5). Indeed, the calculated Ar$_m^*$ metastable atom density
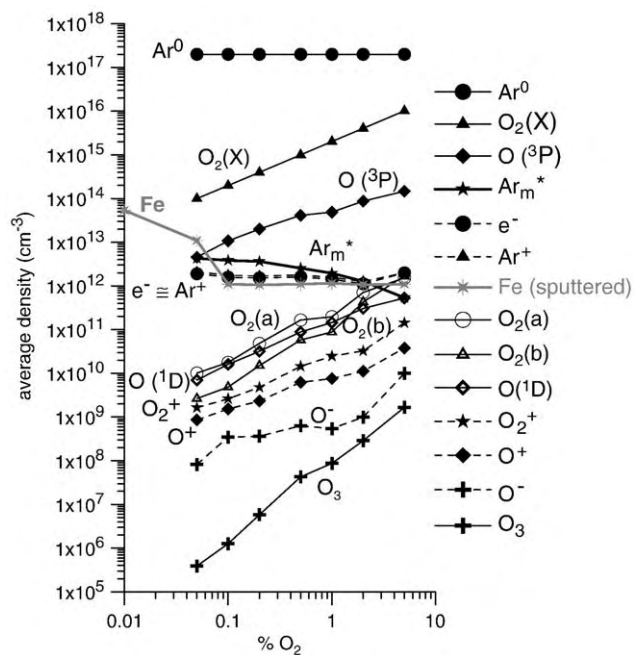
Fig. 5. Calculated densities of all plasma species, taken at the cell axis and averaged in the axial direction, as a function of O_2 concentration. The other conditions are the same as in Fig. 2.

clearly drops upon O_2 addition, as is illustrated by the thick solid line in Fig. 5. This is due to the important loss mechanism of Ar_m^* quenching upon collision with O_2 molecules (reaction 86 of Table 4; see also discussion above and Table 5). Indeed, quenching of Ar_m^* atoms upon dissociation of O_2 molecules was calculated to contribute for nearly 47% to the total loss of the Ar_m^* atoms at 1% O_2 addition, and this relative contribution increases to 72% at 5% O_2 addition.

In a recent paper by Hayashi et al. [80], Ar metastable densities were measured by laser absorption spectroscopy in an Ar/O_2 inductively coupled plasma (ICP) operating at 100 mTorr. It was found that even small abundances of O_2 (~1%) lead to significant increases in the metastable density, mostly due to the reduction of the electron density, since electron-induced quenching was found the dominant loss mechanism of the Ar metastables. Only at O_2
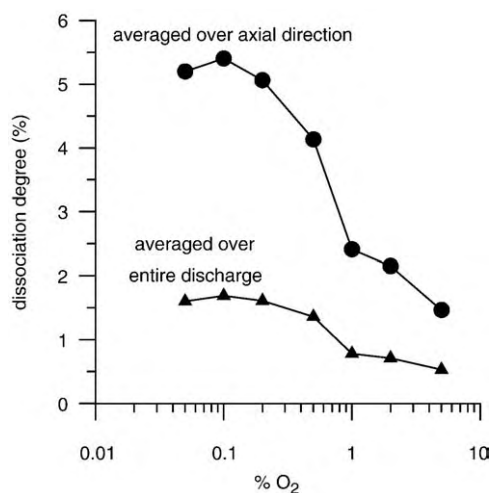
Fig. 6. Calculated O_2 dissociation degree, both taken at the cell axis and averaged in the axial direction, as well as averaged over the entire discharge, as a function of O_2 concentration. The other conditions are the same as in Fig. 2.

abundances above 7–15% (depending on the power), quenching by O_2 molecules started to dominate, and the Ar metastable density dropped again. This observation is opposite to our model predictions, but under such conditions (ICP at 100 mTorr) the electron density is typically quite high, so that electron quenching can indeed be the dominant loss process. It is probably not wise to compare both results, because of totally different plasma conditions. In other papers, e.g., [27] it was also found, for an Ar/O_2 cc rf discharge at 250 mTorr, that the Ar metastable density dropped upon addition of 1% O_2 concentration, due to quenching by O_2 molecules and O atoms. The same effect, i.e., decreasing Ar_m^* density upon addition of gas impurities, was also observed in our earlier model predictions for Ar/H_2 [41–43] and Ar/N_2 [44] GDs.

The average Ar_m^* metastable density is quite comparable to the average electron and Ar^+ ion densities, as is clear from Fig. 5, but the latter do not change a lot upon O_2 addition. Only for O_2 concentrations above 1%, the Ar^+ ion density starts to drop, due to the upcoming of O^+ and O_2^+ ions, and the quasi-neutrality condition in the NG region. Note that the average electron density is slightly lower than the average Ar^+ ion density, because the latter is small but non-zero in the CDS, whereas the electron density is virtually zero in this region (see Fig. 2(a, b) above).

The average densities of the O_2 molecules and O atoms in the excited levels (i.e., $O_2(a)$, $O_2(b)$ and $O(^1D)$) appear to be in the same order, and they rise nearly linearly with O_2 addition, which is like expected, as they are directly formed out of the O_2 gas. In ref. [15] it was also reported that the $O(^1D)$, $O_2(a)$ and $O_2(b)$ densities were comparable to each other in an Ar/O_2 magnetron discharge.

Also the O_2^+, O^+ and O^- ion densities clearly rise for higher O_2 concentrations, but their densities are slightly lower than the excited level populations. The O_2^+ density is a bit higher than the O^+ density, because of the somewhat higher collision rate of electron impact ionization of O_2 compared to electron impact dissociative ionization (cf. the cross sections in Fig. 1 above), and because of the additional important production by asymmetric charge transfer with Ar^+ ions (see above). A factor of two difference in the O^+ and O_2^+ densities was also reported in [14] for an Ar/O_2 magnetron discharge. The O^- ion density is still about one order of magnitude lower than the O^+ ion density.

The average density of the O_3 molecules is still a few orders of magnitude lower than for the other species, but it increases significantly upon O_2 addition. It is expected that the O_3 concentration becomes higher for higher gas pressures, because of the increasing importance of three-body collisions.

Finally, we have also added to Fig. 5 the calculated sputtered (Fe) atom density, again averaged over the axial direction. The Fe atom density is calculated in the same way as in our previous models (e.g., [77]), i.e., the sputter flux is calculated from the energy distributions of the species bombarding the cathode, multiplied with the sputter yield as a function of bombarding energy, as obtained from the empirical Matsunami formula [81]. The sputtered atoms arrive in the plasma with typical energies of a few eV, which they lose rapidly by collisions, until they are thermalized. This thermalization process is simulated with a Monte Carlo model [82]. The further transport of the sputtered atoms is diffusion-dominated. Furthermore, they can become excited and ionized. The behavior of these thermal sputtered atoms, the corresponding ions and excited atoms is described with a fluid model [77].

It is experimentally observed that O_2 addition to an Ar GD results in a dramatic drop in the sputtering rates [5,7–10]. This effect can partly be explained by the fact that oxygen ions are less efficient in sample sputtering, because of their lower masses [5]. However, it can also be attributed to the formation of a thin oxide layer on the cathode surface, due to the bombardment of oxygen species [5]. This phenomenon is also well known in reactive magnetron sputtering, and is called "poisoning". In [83] it was stated that the sputter yield of Ti from a poisoned (TiO_x) target is almost 9 times lower than the

sputter yield of Ti on a pure metal target. Poisoning was assumed to be "complete" already at 2% O_2 addition [17]. Fischer et al. reported that the oxide layer was fully developed at an O_2 concentration of 1.5% [5]. On the other hand, previous experiments (e.g., [8]) seem to indicate that the sputtering rates for a metallic sample in an Ar/O_2 discharge are lower than for a glass sample (made of metallic oxides) in an Ar discharge. This suggests that the formation of the oxide layer is not the only reason for the drop in the sputtering rates upon O_2 addition, but also the less efficient sputtering due to bombarding oxygen ions, as mentioned above [5].

Mushtaq et al. have measured sputtering rates of Fe in an Ar/O_2 Grimm-type GD [10]. They observed a dramatic decrease in the sputtering rate upon O_2 addition. From these measurements, at 700 V and 10 mA, i.e., not too far from the conditions under study in our model, we can deduce that the sputtering rate has dropped already by a factor of 5 at 0.05% O_2 addition, and by a factor of 50 at 0.1% of O_2 addition. This suggests that the so-called "poisoning" already occurs at O_2 additions as low as 0.05%. We have deduced the decrease in Fe sputter yields upon O_2 addition based on these experimentally observed drops in the sputtering rates.

The calculated sputtered Fe atom densities, again taken at the cell axis and averaged over the axial direction, are plotted against O_2 concentration in Fig. 5 (gray line). The point at 0.01% O_2 is taken as the reference for a pure Ar discharge, hence assuming no poisoning yet at 0.01% O_2 addition. It is indeed clear that the sputtered atom density drops significantly, already at very small O_2 concentrations of 0.05 and 0.1%, after which it stays more or less constant, as we assume that the poisoning is complete [17,83].

By comparing the sputtered Fe atom densities with the densities of the other plasma species, we can conclude that the sputtered atom density is comparable to the $O(^3P)$ ground state density at the very low O_2 concentration of 0.05%, but it becomes significantly lower, and comparable to the electron and Ar^+ ion density, at higher O_2 concentrations. This might have important consequences for the optical emission intensities of the sputtered atoms, which will also drop upon O_2 addition. The latter is indeed confirmed by experiments (e.g., [5,7,8,10]), although the drop in emission intensities seems not so pronounced as the drop in sputtering rates. This suggests that the excitation efficiency of the sputtered atoms in the Ar/O_2 discharge is probably higher than in a pure Ar discharge, which might be attributed to either enhanced electron impact excitation, or (more probably) to enhanced excitation due to oxygen species (e.g., asymmetric charge transfer with O^+ or O_2^+ ions, or energy transfer from excited O levels into excited analyte levels). It would be interesting to investigate such mechanisms in the future, by looking in more detail at the analyte emission yields for a large number of lines.

4. Conclusion

We have developed a hybrid model for an Ar/O_2 dc GD, consisting of a Monte Carlo model for the electrons and fluid models for the other plasma species. The following species are considered in the model: Ar atoms in the ground state and the metastable level, O_2 gas molecules in the ground state and two metastable levels, O atoms in the ground state and one metastable level, O_3 molecules, Ar^+, O^+, O_2^+ and O^- ions, as well as the electrons. In total, 87 different reactions between the various plasma species are taken into account.

Besides the 2D density profiles of the various plasma species, information is also given on the relative importance of their production and loss processes, as well as on the dissociation degree of oxygen. It is found that the dissociation degree is in the order of a few %, for the conditions under investigation. The O_2 molecules in the metastable levels ($O_2(a)$ and $O_2(b)$) as well as the O atoms in the metastable level ($O(^1D)$) are of comparable magnitude, which is about 3–4 orders of magnitude lower than the densities of the $O_2(X)$ and $O(^3P)$ ground state species. The O_3 density is still more than 3

orders of magnitude lower. Concerning the ionic species, the Ar^+ ions are still dominant, which is logical as the O_2 gas is only present as a minor constituent. The O_2^+ ions are about twice as important as the O^+ ions. The O^- ion density is about one order of magnitude lower than the O^+ ion density.

The effect of different O_2 additions, in the range between 0.05 and 5%, on the calculated species densities is investigated. All oxygen species increase nearly linearly upon O_2 addition. On the other hand, the Ar_m^* metastable density decreases clearly for higher O_2 concentrations, which is attributed to the growing importance of Ar_m^* quenching upon collision with O_2 molecules. The latter process is also found to be the main dissociation mechanism for the O_2 molecules. Hence, the drop in Ar_m^* density upon O_2 addition explains the decreasing trend in the dissociation degree with rising O_2 concentrations. Finally, the sputtered atom density drops also significantly upon O_2 addition, even at very low O_2 concentrations. This can be attributed to the formation of an oxide film on the cathode surface, resulting in a lower sputtering yield. This observation might have important consequences for GDs used in analytical spectrometry.

References

[1] E.B.M. Steers, P. Smid, V. Hoffmann, Z. Weiss, The effects of traces of molecular gases (H_2, N_2 & O_2) in glow discharges in noble gases, J. Phys. C: Conf. Series 133 (2008) 012020.
[2] S. De Gendt, R.E. Van Grieken, S.K. Ohorodnik, W.W. Harrison, Parameter evaluation for the analysis of oxide-based samples with radio frequency glow discharge mass spectrometry, Anal. Chem. 36 (1995) 1026–1033.
[3] A. Bengtson, Depth profiling of organic coatings with GD-OES—investigation of molecular emission and interference, J. Anal. At. Spectrom. 18 (2003) 1066–1068.
[4] A. Bengtson, The impact of molecular emission in compositional depth profiling using glow discharge optical emission spectrometry, Spectrochim. Acta Part B 63 (2008) 917–928.
[5] W. Fischer, A. Naoumidis, H. Nickel, Effects of controlled addition of nitrogen and oxygen to argon on the analytical parameters of glow discharge optical emission spectrometry, J. Anal. At. Spectrom. 9 (1994) 375–380.
[6] K. Wagatsuma, Emission characteristics of mixed gas plasmas in low-pressure glow discharges, Spectrochim. Acta Part B 56 (2001) 465–486.
[7] K. Wagatsuma, K. Hirokawa, Effect of oxygen addition to an argon glow discharge plasma source in atomic emission spectrometry, Anal. Chim. Acta 306 (1995) 193–200.
[8] B. Fernàndez, N. Bordel, C. Pérez, R. Pereiro, A. Sanz-Medel, The influence of hydrogen, nitrogen and oxygen additions to radiofrequency argon glow discharges for optical emission spectrometry, J. Anal. At. Spectrom. 17 (2002) 1549–1555.
[9] B. Fernàndez, N. Bordel, R. Pereiro, A. Sanz-Medel, Investigations of the effect of hydrogen, nitrogen or oxygen on the in-depth profile analysis by radiofrequency argon glow discharge-optical emission spectrometry, J. Anal. At. Spectrom. 18 (2003) 151–156.
[10] S. Mushtaq, J. Pickering and E. Steers, Effects of small quantities of oxygen on intensities of FeI and ArI lines in analytical glow discharges, Oral presentation at the "Colloquium Spectroscopicum Internationale", Budapest, 2009.
[11] M.A. Lieberman, A.J. Lichtenberg, Principles of Plasma Discharges and Materials Processing, Wiley, New York, 1994.
[12] P. Ghekiere, S. Mahieu, G. De Winter, R. De Gryse, D. Depla, Scanning electron microscopy study of the growth mechanism of biaxially aligned magnesium oxide layers grown by unbalanced magnetron sputtering, Thin Solid Films 493 (2005) 129–134.
[13] I. Safi, A novel reactive magnetron sputtering technique for producing insulating oxides of metal alloys and other compound thin films, Surf. Coat. Technol. 135 (2000) 48–59.
[14] W. Trennepohl Jr., J. Bretagne, G. Gousset, D. Pagnon, M. Touzeau, Modelling of an $Ar–O_2$ reactive magnetron discharge used for deposition of chromium oxide, Plasma Sources Sci. Technol. 5 (1996) 607–621.
[15] J. Bretagne, G. Gousset, W. Trennepohl Jr., Plasma–surface interaction modelling of dc reactive magnetron sputtering, Surf. Coat. Technol. 97 (1997) 611–617.
[16] K. Nanbu, K. Mitsui, S. Kondo, Self-consistent particle modeling of dc magnetron discharges of an O_2/Ar mixture, J. Phys. D: Appl. Phys. 33 (2000) 2274–2283.

[17] E. Bultinck A. Bogaerts, Particle-in-cell/Monte Carlo collisions treatment of an Ar/O$_2$ magnetron discharge used for the reactive sputter deposition of TiO$_x$ films, New J. Phys. 11 (2009) 103010.

[18] A. Palmero, N. Tomozeiu, A.M. Vredenberg, W.M. Arnoldbik, F.H.P.M. Habraken, On the deposition process of silicon suboxides by a RF magnetron reactive sputtering in Ar–O$_2$ mixtures: theoretical and experimental approach, Surf. Coat. Technol. 177–178 (2004) 215–221.

[19] A. Lebéhot, J. Kurzyna, V. Lago, M. Dudeck, M. Nishida, Simple model for the electronic relaxation during the expansion of a plasma generated in an Ar–O$_2$ mixture, Phys. Plasmas 6 (1999) 4750–4758.

[20] X.-M. Zhu, Y.-K. Pu, A simple collisional-radiative model for low-pressure argon–oxygen mixture gases, J. Phys. D: Appl. Phys. 40 (2007) 5202–5205.

[21] T. Watanabe, M. Shigeta, N. Atsuchi, Two-temperature chemically-non-equilibrium modeling of argon induction plasmas with diatomic gas, Int. J. Heat Mass Transfer 49 (2006) 4867–4876.

[22] N. Atsuchi, M. Shigeta, T. Watanabe, Modeling of non-equilibrium argon–oxygen induction plasmas under atmospheric pressure, Int. J. Heat Mass Transfer 49 (2006) 1073–1082.

[23] M. Moravej, X. Yang, R.F. Hicks, J. Penelon, S.E. Babayan, A radio-frequency nonequilibrium atmospheric pressure plasma operating with argon and oxygen, J. Appl. Phys. 99 (2006) 093305.

[24] C. Lee, M.A. Lieberman, Global model of Ar, O$_2$, Cl$_2$ and Ar/O$_2$ high-density plasma discharges, J. Vac. Sci. Technol. A 13 (1995) 368–380.

[25] C.-C. Hsu, M.A. Nierode, J.W. Coburn, D.B. Graves, Comparison of model and experiments for Ar, Ar/O$_2$ and Ar/O$_2$/Cl$_2$ inductively coupled plasmas, J. Phys. D: Appl. Phys. 39 (2006) 3272–3284.

[26] T.J. Sommerer, M.J. Kushner, Numerical investigation of the kinetics and chemistry of rf glow discharge plasmas sustained in He, N$_2$, O$_2$, He/N$_2$/O$_2$, He/CF$_4$/O$_2$ and SiH$_4$/NH$_3$ using a Monte Carlo-fluid hybrid model, J. Appl. Phys. 71 (1992) 1654–1673.

[27] S. Rauf, M.J. Kushner, Argon metastable densities in radio frequency Ar, Ar/O$_2$ and Ar/CF$_4$ electrical discharges, J. Appl. Phys. 82 (1997) 2805–2813.

[28] S. Tinck, W. Boullart, A. Bogaerts, Investigation of etching and deposition processes of Cl$_2$/O$_2$/Ar inductively coupled plasmas on silicon by means of plasma-surface simulations and experiments, J. Phys. D: Appl. Phys. 42 (2009) 095204.

[29] S. Tinck A, Bogaerts, paper in preparation.

[30] B. Eliasson, U. Kogelschatz, Basic Data for Modelling of Electrical Discharges in Gases: Oxygen, Asea Brown Boveri Corporate Research, Forschungsbericht KLR 86-11 C, June 1986.

[31] B. Eliasson, M. Hirth, U. Kogelschatz, Ozone synthesis from oxygen in dielectric barrier discharges, J. Phys. D: Appl. Phys. 20 (1987) 1421–1437.

[32] S. Hadj-Ziane, B. Held, P. Pignolet, R. Peyrous, C. Coste, Ozone generation in an oxygen-fed wire-to-cylinder ozonizer at atmospheric pressure, J. Phys. D: Appl. Phys. 25 (1992) 677–685.

[33] S. Panda, D.J. Economou, M. Meyyappan, Effect of metastable oxygen molecules in high density power-modulated oxygen discharges, J. Appl. Phys. 87 (2000) 8323–8333.

[34] G. Gousset, C.M. Ferreira, M. Pinheiro, P.A. Sa, M. Touzeau, M. Vialle, J. Loureiro, Electron and heavy-particle kinetics in the low pressure oxygen positive column, J. Phys. D: Appl. Phys. 24 (1991) 290–300.

[35] M.J. Pinheiro, G. Gousset, A. Granier, C.M. Ferreira, Modelling of low-pressure surface wave discharges in flowing oxygen: I. Electrical properties and species concentrations, Plasma Sources Sci. Technol. 7 (1998) 524–536.

[36] V. Guerra, J. Loureiro, Non-equilibrium coupled kinetics in stationary N$_2$–O$_2$ discharges, J. Phys. D: Appl. Phys. 28 (1995) 1903–1918.

[37] V. Guerra, J. Loureiro, Self-consistent electron and heavy-particle kinetics in a low-pressure N$_2$–O$_2$ glow discharge, Plasma Sources Sci. Technol. 6 (1997) 373–385.

[38] V. Guerra, J. Loureiro, Kinetic model of a low-pressure microwave discharge in O$_2$–N$_2$ including the effects of O$^-$ ions on the characteristics for plasma maintenance, Plasma Sources Sci. Technol. 8 (1999) 110–124.

[39] M. Mrazkova, P. Vasina, V. Kudrle, A. Talsky, C.D. Pintassilgo, V. Guerra, On the oxygen addition into nitrogen post-discharges, J. Phys. D: Appl. Phys. 42 (2009) 075202.

[40] I.A. Kossyi, A. Yu Kostinky, A.A. Matveyev, V.P. Silakov, Kinetic scheme of the non-equilibrium discharge in nitrogen–oxygen mixtures, Plasma Sources Sci. Technol. 1 (1992) 207–220.

[41] A. Bogaerts, R. Gijbels, Hybrid Monte Carlo-fluid modeling network for an argon/hydrogen direct current glow discharge, Spectrochim. Acta Part B 57 (2002) 1071–1099.

[42] A. Bogaerts, R. Gijbels, Effect of small amounts of hydrogen added to argon glow discharges: hybrid Monte Carlo-fluid model, Phys. Rev. E 65 (2002) 056402.

[43] A. Bogaerts, Computer simulations of argon–hydrogen Grimm-type glow discharges, J. Anal. At. Spectrom. 23 (2008) 1441–1556.

[44] A. Bogaerts, Hybrid Monte Carlo-fluid model for studying the effects of nitrogen addition to argon glow discharges, Spectrochim. Acta Part B 64 (2009) 126–140.

[45] A. Bogaerts, M. van Straaten, R. Gijbels, Monte Carlo simulation of an analytical glow discharge: motion of electrons, ions and fast neutrals in the cathode dark space, Spectrochim. Acta Part B 50 (1995) 179–196.

[46] E.W. McDaniel, E.A. Mason, The Mobility and Diffusion of Ions in Gases, John Wiley & Sons, New York, 1973.

[47] R.C. Reid, J.M. Prausnitz, B.E. Poling, The Properties of Gases and Liquids, 4 ed. McGraw-Hill, New York, 1987.

[48] R.A. Svehla, Estimated viscosities and thermal conductivities of gases at high temperatures, National Aeronautics and Space Administration, Washington DC, 1962.

[49] A. Bogaerts, R. Gijbels, W.J. Goedheer, Hybrid Monte Carlo-fluid model of a direct current glow discharge, J. Appl. Phys. 78 (1995) 2233–2241.

[50] A.V. Phelps, Z. Lj, Petrovic, cold-cathode discharges and breakdown in argon: surface and gas phase production of secondary electrons, Plasma Sources Sci. Technol. 8 (1999) R21–R44.

[51] N.J. Mason, W.R. Newell, Total cross sections for metastable excitation in the rare gases, N. J. Mason and J. Phys. B 20 (1987) 1357–1377.

[52] H.A. Hyman, Electron-impact ionization cross sections for excited states of the rare gases (Ne, Ar, Kr, Xe), cadmium and mercury, Phys. Rev. A 20 (1979) 855–859.

[53] H.A. Hyman, Electron-impact excitation of metastable argon and krypton, Phys. Rev. A 18 (1978) 441–446.

[54] A.V. Phelps: ftp://jila.colorado.edu/collision_data.

[55] K.N. Joshipura, P.M. Patel, Cross sections of e$^-$—O scattering at intermediate and high energies (E_i=8.7–1000 eV), Phys. Rev. A 48 (1993) 2464–2467.

[56] R.R. Laher, F.R. Gilmore, Updated excitation and ionization cross sections for electron impact on atomic oxygen, J. Phys. Chem. Ref. Data 19 (1990) 277–305.

[57] S. Hashiguchi, Numerical calculations for the electron energy distribution in a He hollow-cathode glow discharge, IEEE Trans. Plasma Science 19 (1991) 297–300.

[58] Appl. Atom. Coll. Phys. in: W.L. Nighan (Ed.), Gas Lasers, vol. 3, Academic Press, New York, 1982, Chapter 6.

[59] F. Howorka, Reactions in singly and doubly charged argon ions with N$_2$ and O$_2$ in a steady state hollow cathode discharge, J. Chem. Phys. 68 (1978) 804–811.

[60] C. Rebrion, B.R. Rowe, J.B. Marquette, Reactions of Ar$^+$ with H$_2$, N$_2$, O$_2$ and CO at 20, 30 and 70 K, J. Chem. Phys. 91 (1989) 6142–6147.

[61] D.C. Parent, R. Derai, G. Mauclaire, M. Heninger, R. Marx, M.E. Rincon, A. O'Keefe, M.T. Bowers, Comparison of energy partitioning in Ar$^+$ and N$_2^+$ charge transfer reactions, Chem. Phys. Lett. 117 (1985) 127–131.

[62] W. Lindinger, E. Alge, H. Störi, M. Pahl, R.N. Varney, Flow-drift tube investigation of some Ar^{++} reactions, J. Chem. Phys. 67 (1977) 3495–3499.

[63] J.Y. Jeong, J. Park, I. Henins, S.E. Babayan, V.J. Tu, G.S. Selwyn, G. Ding, R.F. Hicks, Reaction chemistry in the afterglow of an oxygen–helium atmospheric pressure plasma, J. Phys. Chem. A 104 (2000) 8027–8032.

[64] R.J. Donovan, D. Husain, Recent advances in the chemistry of electronically excited atoms, Chem. Rev. 70 (1970) 489–516.

[65] C.M. Ferreira, A. Ricard, Modelling of the low-pressure argon positive column, J. Appl. Phys. 54 (1983) 2261–2271.

[66] C.M. Ferreira, J. Loureiro, A. Ricard, Populations in the metastable and the resonance levels of argon and stepwise ionization effects in a low-pressure argon positive column, J. Appl. Phys. 57 (1985) 82–90.

[67] L.A. Riseberg, W.F. Parks, L.D. Schearer, Penning ionization of Zn and Cd by noble-gas metastable atoms, Phys. Rev. A 8 (1973) 1962–1968.

[68] S. Inaba, T. Goto, S. Hattori, Determination of the Penning excitation cross sections of Mg atoms by He, Ne and Ar metastable atoms, J. Phys. Soc. Jpn 52 (1983) 1164–1167.

[69] K. Tachibana, Excitation of the 1s$_5$, 1s$_4$, 1s$_3$ and 1s$_2$ levels of argon by low-energy electrons, Phys. Rev. A 34 (1986) 1007–1015.

[70] L.G. Piper, J.E. Velazco, D.W. Setser, Quenching cross sections for electronic energy transfer reactions between metastable argon atoms and noble gases and small molecules, J. Chem. Phys. 59 (1973) 3323–3340.

[71] M. Bourène, J. Le Calvé, De-excitation cross sections of metastable argon by various atoms and molecules, J. Chem. Phys. 58 (1973) 1452–1458.

[72] J.E. Velazco, J.H. Kolts, D.W. Setser, Rate constants and quenching mechanisms for the metastable states of Ar, Kr and Xe, J. Chem. Phys. 69 (1978) 4357–4373.

[73] M. Mozetic, U. Cvelbar, Determination of the neutral oxygen atom density in a plasma reactor loaded with metal samples, Plasma Sources Sci. Technol. 18 (2009) 034002.

[74] K. Kutasi, J. Loureiro, Role of the wall reactor material on the species density distributions in an N$_2$–O$_2$ post-discharge for plasma sterilization, J. Phys. D: Appl. Phys. 40 (2007) 5612–5623.

[75] A. Bogaerts, R. Gijbels, Comprehensive description of a Grimm-type glow discharge source used for optical emission spectrometry: a mathematical simulation, Spectrochim. Acta Part B 53 (1998) 437–462.

[76] A. Bogaerts, The afterglow mystery of pulsed glow discharges and the role of dissociative electron-ion recombination, J. Anal. At. Spectrom. 22 (2007) 502–512.

[77] A. Bogaerts, R. Gijbels, Two-dimensional model of a direct current glow discharge: description of the argon metastable atoms, sputtered atoms and ions, Anal. Chem. 68 (1996) 2676–2685.

[78] A. Bogaerts, Z. Donko, K. Kutasi, G. Bano, N. Pinhao, M. Pinheiro, Comparison of calculated and measured optical emission intensities in a direct current argon–copper glow discharges, Spectrochim. Acta Part B 55 (2000) 1465–1479.

[79] K. Kutasi, V. Guerra, P. Sa, J. Loureiro, Active species in Ar–O$_2$ and Ar–O$_2$–N$_2$ flowing microwave discharges and post-discharges, in: A. von Keudell, J. Winter, M. Böke, V. Schulz von der Gathen (Eds.), Proceedings of the "19th International Symposium on Plasma Chemistry", 2009.

[80] Y. Hayashi, S. Hirao, Y. Zhang, T. Gans, D. O'Connell, Z. Lj. Petrovic, T. Makabe, Argon metastable state densities in inductively coupled plasma in mixtures of Ar and O$_2$, J. Phys. D: Appl. Phys. 42 (2009) 145206.

[81] N. Matsunami, Y. Yamamura, Y. Itikawa, N. Itoh, Y. Kazumata, S. Miyagawa, K. Morita, R. Shimizu, H. Tawara, Energy dependence of the ion-induced sputtering yields of monoatomic solids, Atom. Data Nucl. Data Tables 31 (1984) 1–79.

[82] A. Bogaerts, M. van Straaten, R. Gijbels, Description of the thermalization process of the sputtered atoms in a glow discharge, using a three-dimensional Monte Carlo method, J. Appl. Phys. 77 (1995) 1868–1874.

[83] D. Depla, S. Mahieu, R. De Gryse, Magnetron sputter deposition: linking discharge voltage with target properties, Thin Solid Films 517 (2009) 2825–2839.